Applied Thermal Engineering 268 (2025) 125835

Contents lists available at ScienceDirect

Applied Thermal Engineering

journal homepage: www.elsevier.com/locate/ate

Research Paper

Predictive fuel cell thermal management for fuel cell electric tractors

Christian Varlese [a,*], Maximilian Haslinger [a], Christian Junger [a], Johannes Konrad [a], Rudolf Krizan [a], Christoph Hametner [b], Peter Hofmann [a]

[a] Institute of Powertrain and Automotive Technology, TU Wien, Vienna, Austria
[b] Christian Doppler Laboratory for Innovative Control and Monitoring of Automotive Powertrain Systems, TU Wien, Vienna, Austria

ARTICLE INFO

Keywords:
Thermal management
Fuel cell electric vehicle
Fuel cell agricultural machinery
Model predictive control

ABSTRACT

This study addresses the significant challenges associated with adopting fuel cell powertrains for agricultural machinery, particularly concerning efficiency and durability due to the demanding operational environment. A critical factor is the fuel cell's operational temperature, which can lead to degradation, higher auxiliary consumption, and larger radiator volumes. To mitigate these problems, the present study introduces a predictive control approach for thermal management. Specifically, the notable advantages of the non-linear model predictive controller over classical control approaches can be attributed to the combination of a control-oriented model and predictions into a real-time optimization problem. This approach stands as an innovative addition aimed at compensating the inertia of the cooling system while deploying predictions to improve the control accuracy and concurrently optimize the utilization of actuators. This work is organized into two principal contributions: the extensive modeling of a fuel cell system and its validation, and the comprehensive investigation of a model predictive control strategy. The results demonstrate that a predictive thermal management strategy can significantly diminish auxiliary consumption by up to 30% compared to classical control strategies across various ambient temperatures without compromising temperature reference control. In particular, a comparison with a classical control strategy reveals the effective deployment of multiple actuators and prediction under the prescribed constraints in the proposed control concept. Additionally, the study quantifies the impact of ambient temperature on auxiliary consumption and identifies operational scenarios where model predictive control performs optimally. As part of the unique contribution of this work, the cost function weights, length, and accuracy of the prediction horizon are also analyzed, with findings showing that a balance between performance and actuator consumption can be achieved.

1. Introduction

The present study proposes a predictive control strategy for fuel cell thermal management. In response to the adverse consequences of imbalanced development, the call for sustainable growth has become universal, addressing every sector of human activities [1]. In connection with this movement, the importance of sustainable farming practices has risen significantly within a vast majority of our society [2]. Consequently, regulatory standards pertaining to emissions for non-road machinery have been subject to a stringent tightening of limits [3] and have propelled significant efforts towards the electrification of agricultural machinery [4]. Within this context, the integration of proton-exchange-membrane (PEM) fuel cell powertrains in tractors has consistently demonstrated advantages across various prototypes, attributed to their high gravimetric density and rapid refueling capabilities [5]. In recent years, several advancements in materials science have been made to increase the thermal stability of fuel cells [6,7]. Nevertheless, the widespread commercialization of fuel cell powertrains in tractors encounters substantial obstacles. These hurdles are attributable to shorter component lifespans and elevated fuel expenses [8]. One critical factor influencing both the degradation and efficiency of a fuel cell is its operational temperature. The research by [9–11] highlights key factors influencing fuel cell performance degradation. Elevated temperatures can degrade the membrane structure and cause platinum dissolution in the catalyst layer. High temperatures may also reduce relative humidity, promoting radical formation in the membrane, while lower humidity accelerates catalyst layer dissolution and carbon support corrosion. However, the reduction of the fuel cell operating temperature can have repercussions on the overall system performance: the lower temperature difference between ambient and fuel cell requires an increase of auxiliary power [12]. Achieving a delicate balance between these two concurring goals is crucial for

* Corresponding author.
E-mail address: christian.varlese@ifa.tuwien.ac.at (C. Varlese).

https://doi.org/10.1016/j.applthermaleng.2025.125835
Received 18 November 2024; Received in revised form 4 January 2025; Accepted 2 February 2025
Available online 10 February 2025

optimal performance and typically, this equilibrium is found within a temperature range of 60 to 80 °C [13]. Managing the operational temperature stands out as one of the most complex aspects of fuel cell thermal management strategies (TMSs), given that a substantial portion of the waste heat must be dissipated through a cooling system [14]. This aspect represents a critical distinction from traditional internal combustion engines, where higher operating temperatures and larger quantities of exhaust gas even enable waste heat recovery, thereby improving efficiency [15]. This is exacerbated by the performance characteristics of the fuel cell stack, wherein efficiency decreases with the load, consequently leading to an increase in waste heat [16]. Meeting the heightened cooling requirements necessitates an expansion in the radiator surface area and an increase in the air mass flow rate through the fans in comparison with conventional powertrains [17,18]. As a consequence, the enlarged dimensions contribute to heightened inertia within the thermal system and introduce delays in the response of the actuator. This challenge is notably pronounced in tractors, where the presence of airstream is nearly absent: during farming activities, tractors often operate at higher loads, maintaining an average speed of approximately 4 km/h according to [19,20].

1.1. Literature survey

The temperature control of PEM fuel cells has received considerable attention in the last two decades. Initial investigations primarily employed classical control methods, such as the proportional–integral–derivative controller (PID controller) [21,22], rule-based approaches [23] and state feedback [24]. These investigations revealed significant challenges associated with system dynamics, non-linearity and optimal performance of the actuators related to PEM fuel cell systems. Consequently, there has been a shift towards more advanced control strategies, including feedforward techniques [25], fuzzy logic algorithms [26–28], and model-reference control [29] to effectively manage system dynamics and non-linearities. Approximately a decade ago, model predictive controller (MPC) was already under scrutiny for solid oxyde fuel cells [30,31], highlighting the advantages of incorporating prediction in the control problem, particularly for systems with high inertia. Following this, the introduction of model-based control methods also gained prominence in PEM research. Specifically, in [32], MPC was applied to control fans, while in [33], it was employed for pump and bypass valve regulation. Furthermore, Liu et al. [34] extended MPC to concurrently regulate fans, and bypass valves. Offline optimization techniques, such as rolling optimization with model-predictive control [35], have emerged, especially for fan control. [36] investigated the integration of an MPC controller for the thermostat with feedforward controllers for the pump and fan on a testbed. Similarly, [37] developed an MPC framework to control the fans of a PEM fuel cell. In [38], an MPC framework was implemented to calculate the setpoint targets for a PID controller. [39] highlighted the benefits of integrating the pump and fan actuators within the MPC formulation to regulate temperature during a typical passenger car cycle. [40] explored similar advantages by combining the fan, pump, thermostat, and heater in laboratory cycles. Additionally, in [41], dynamic programming methods have been explored, demonstrating the advantages of utilizing and optimizing all actuators in the system: fans, bypass valve, and pump. A summary of the discussed literature is presented in Table 1.

The current investigation introduces a model predictive controller as a solution to the challenges outlined earlier. The extensive modeling of the fuel cell stack and thermal system accentuates the inherent inertia of the overall system due to the considerable size of actuators and components. Furthermore, an analysis is conducted on classical control approaches, presently representing state-of-the-art implementations. Limitations in terms of response time and accuracy are evident in error-value controlled systems, such as PID controllers, when applied to complex systems with non-linearities or substantial inertia, such as heavy-duty fuel cell thermal systems. Typically, traditional PID controllers lack an inherent mechanism for coordinating multiple actuators simultaneously. Each term in the PID controller contributes to the control signal, influencing the behavior of the single actuator to which it is assigned. The proposed non-linear MPC addresses the significant inertia of the heavy-duty fuel cell stack and optimizes the usage of fans and pumps by integrating a control-oriented model and predictions into a real-time optimization problem. A key contribution of this study involves investigating the potential of model predictive control for a large fuel cell system, considering three duty cycles to identify optimal controller performance conditions. The study demonstrates that the proposed controller significantly reduces actuator energy consumption without compromising control accuracy. Moreover, the analysis explores the impact of operating parameters on the controller's performance, such as cost function weights, ambient temperature, prediction horizon and prediction accuracy, highlighting the controller's performance under various conditions.

1.2. Contribution

This work makes key contributions by integrating pump and fan control into a single MPC framework, analyzing the effects of prediction horizon length, cost function weights, and ambient temperature on MPC performance, and applying MPC to a 132-kW fuel cell system for tractors, a field not widely explored. In particular, the examination of existing literature highlights the unaddressed topics in the field of TMSs for PEM fuel cells as well as the novelty of this work:

- The characteristics of a real heavy-duty fuel cell system, including waste heat and actuators, have not been fully analyzed and modeled in view of TMSs.
- The limited exploration of the combined control of pumps and fans in fuel cell systems.
- The lack of studies addressing predictive control for heavy-duty fuel cell systems in agricultural applications.
- The influence of various conditions on MPC, such as load level, cost function weights, ambient temperature, prediction horizon, and accuracy, has not been quantified yet for real applications.

In order to bridge the identified research gaps, this study introduces an MPC designed for the pump and fans within the fuel cell thermal system. Specifically, the system model was constructed utilizing comprehensive testbed measurements and employed to evaluate the performance of MPC under different loads and ambient temperatures. The objective of this analysis is to ascertain the optimal operating conditions wherein MPC demonstrates high efficacy.

The investigations within the current work call attention to four main findings:

1. The 132-kW fuel cell unit and its PID controllers are examined to underscore the challenges of traditional control strategies. The analysis of the waste heat generated by the fuel cell system underscores the necessity for the thermal management system to dissipate approximately 100 kW even under high ambient temperatures. This entails the use of larger radiators and substantial fans, which possess significant inertia. Furthermore, contemporary controllers, such as PID controllers, mainly rely on deviations from the prescribed inlet temperature, potentially leading to delayed controller responses.
2. The integration of both the pump and fans within the model-based controller highlights the considerable advantages of formulating an optimization problem using two actuators. Through the strategic allocation of weights in the MPC formulation, potential instabilities in inlet temperature resulting from the simultaneous control of the pump and fans are mitigated. Additionally, the effective synergy between these two actuators leads to a reduction in auxiliary consumption, an increase of control accuracy, and a shorter response time.

Table 1
Summary of relevant TMSs for PEM fuel cell in literature showing the novelty of present work. Abbreviations: not applicable (NA), proportional controller (P), passenger car (PC), rule-based controller (RB), state-feedback controller (SF), feed-forward controller (FF), fuzzy-logic controller (FL), model-reference adaptive control (MRAC), model-predictive control (MPC). For each TMS type, the controlled actuator is specified in brackets.

Ref.	Application/Stack power	TMS type (actuators)	MPC parameters variations
[21]	NA/NA	P (fan)	NA
[22]	NA/5 kW	PID (pump)	NA
[23]	PC/30 kW	RB (fan, pump)	NA
[24]	PC/75 W	PI (fan), SF (pump, BPV)	NA
[25]	NA/21 kW	PID (fan), FF (pump)	NA
[26]	NA/NA	FL (pump)	NA
[27]	PC/30 kW	FL-PID (fan, pump)	NA
[28]	NA/NA	FL (fan)	NA
[29]	PC/45 W	MRAC (pump, BPV)	Amb. temperature
[32]	PC/1 kW	MPC (fan)	NA
[33]	NA/50 kW	MPC (pump, BPV)	Prediction horizon Control horizon
[34]	PC/60 kW	MPC (fan, BPV), FF (pump)	Prediction horizon
[35]	Truck/80 kW	MPC (fan)	NA
[36]	NA/85 kW	MPC (BPV), FF (fan, pump)	Prediction horizon
[37]	NA/5 kW	MPC (fan)	Amb. temperature
[38]	NA/5 kW	PID (fan, pump)	NA
[39]	PC/68 kW	MPC (fan, pump)	NA
[40]	Bus/40 kW	MPC (pump, BPV, fan)	Prediction horizon Sample time
[41]	PC/55 kW	DP (fan, pump, BPV)	NA
This work	**Tractor/132 kW**	**MPC (fans, pump)**	**Cost weights** **Amb. temperature** **Prediction horizon** **Prediction accuracy**

3. The investigation of predictive TMS for the fuel cell tractor demonstrates the benefits in mitigating auxiliary consumption. In agriculture, farm-related tasks are distinguished by a sequence of high-load phases in the field, followed by lower loads when the tractor nears a curve at the headland, where land is left unploughed. The implementation of pattern recognition techniques may even allow for the acquisition of highly precise load forecasts, which can be deployed by a predictive TMS to reduce fuel consumption and tackle temperature management at low speed.
4. The efficacy of the proposed strategy is assessed across diverse agricultural duties, cost function weights, ambient temperature conditions, and prediction parameters to comprehensively demonstrate the potential of MPC in controlling the thermal systems of fuel cell electric tractors. It is found that the MPC demonstrates optimal performance under mild ambient temperatures and moderate to high workload, as well as effectiveness even under hot ambient temperatures. The variation in cost function weights reveals that while the MPC achieves higher reference-tracking performance, it results in a consistent increase in auxiliary power consumption. Additionally, the analysis of prediction horizon length and accuracy reveals variations in controller performance, a limited increase in computational time, and the necessary accuracy for prediction.

The remainder of this paper is structured as follows. Section 2 describes the fuel cell system on the testbed and the models validated with the experimental data and the losses analysis of the fuel cell stack. Section 3 presents the control strategies of the thermal system including the formulation of the MPC. Section 4 discusses the advantages of the proposed strategy under various power loads, ambient temperature conditions, prediction horizon lengths and accuracy. Finally, Section 5 concludes this work and outlines the potential direction of further research.

2. Fuel cell system testbed set-up and model

In this section, the fuel cell unit was modeled to represent the real system on the testbed. The testbed setup and models were specifically developed to validate the proposed control strategies and evaluate their performance under real-world conditions. Successively, this model is used as the plant model in this study's investigations to assess the performance of the controllers. The fuel cell model was created and validated through extensive measurements at the testbed. This model comprises an equivalent electrical circuit for the fuel cell stack and lump model with four volumes for the thermal system. The validation of the model is a crucial step for the investigations and comparison of control strategies of Section 3.

2.1. Fuel cell system set-up on testbed

The fuel cell unit examined in this work has been employed in the frame of the project "FCTRAC" [18], where a STEYR 4130 Expert CVT, originally a diesel tractor with a net power-take-off power of 95 kW, has been retrofitted with a fuel cell powertrain [42]. The project goal is to power a fuel cell electric tractor using hydrogen produced from local biomass, thereby promoting a circular economy [43]. The 132-kW stack nominal power was chosen to enable hydrogen-powered operation under all conditions while minimizing the high-voltage battery size. The powertrain of the fuel cell tractor was arranged in a testbed for hydrogen systems as illustrated in Varlese et al. [44].

A schematic of the fuel cell system testbed set-up and architecture is depicted in Fig. 1. A summary of the most important specifications is reported in Table 2. The presented testbed setup replicates the

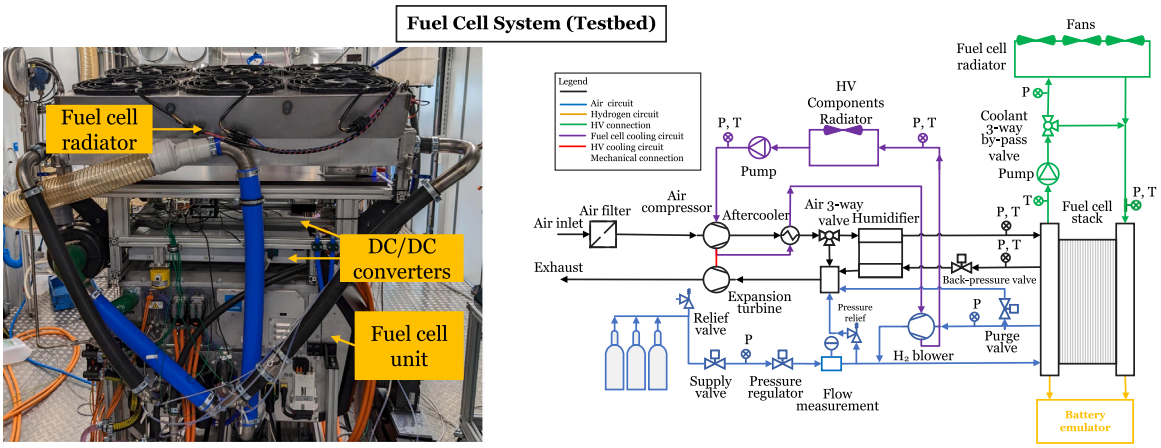

Fig. 1. Fuel cell unit testbed set-up (left) and schematic (right).

Table 2
Summary of relevant fuel cell components specifications.

Component	Description	Specification
Fuel cell stack	Nominal power	132 kW (BoL)
	Nominal current	360 A
	Cells	560
	Cell active area	250 cm^2
Fuel cell unit	Electric net power (excluding HV thermal system)	112 kW
BoP max. power	Compressor	16 kW
	Hydrogen recirculation blower	1 kW
	Fuel cell Coolant pump	1.2 kW
	Fuel cell radiator fans	3.3 kW
	HV components radiator fan	1.1 kW
	HV components pump	0.5 kW
Testbed hydrogen supply	Pressure	(8–300) bar

operating conditions of a tractor. The fuel cell varying load is based on the power demand of the tractor's electric motor and is replicated by the battery emulator, which follows the given setpoint of current. The testbed climatic chamber provides precise control of ambient temperature between 15 and 35 °C, with a constant humidity of 50%, ensuring test repeatability under various conditions or test under precise conditions. The fuel cell stack is rated with a maximum power of 132 kW Beginning-of-Life (BoL). The maximum power of the Balance-of-Plant (BoP) was measured with a constant coolant inlet temperature 60 °C and ambient temperature 20 °C at the testbed. The fuel cell unit's net power is rated at 112 kW, where the air compressor contributes to approx. 75% of BoP components consumption. It must be noted the net power is strictly dependent on the ambient temperature. Therefore, the power difference between stack and unit does not necessarily correspond to the sum of the maximum power of the BoP components. Furthermore, the auxiliaries of the HV components cooling circuits are not taken into account in this calculation. In comparison to the power electronics of the entire powertrain, the high-voltage fuel cell components contribute a negligible amount of waste heat to the overall cooling circuit, which is, therefore, dominated by the waste heat from other components.

The following subsections describe the model derived from the testbed measurements. A schematic of the model is shown in Fig. 2. Here, it can be seen the model consists of two submodels: the fuel cell stack electrochemical model and the thermal system lumped model. It must be stressed the electrochemical model allows an accurate representation of the voltage in transient behavior, which is of pivotal importance for the unsteady characterization of the stack waste heat.

2.2. Fuel cell stack electrochemical model and validation

A single-cell electrochemical model is employed to accurately represent the steady and transient characteristics of the actual stack waste heat in the coolant P_{cool} and to evaluate the losses in the stack. The model is based on an equivalent electrical circuit of Wang [45] partially parametrized with literature data from [46,47]. The fuel cell stack model is derived from the multiplication of the cell voltage output with the number of cells in the stack.

The cell voltage V_{cell} is expressed through the equivalent electrical circuit of Fig. 2 as follows

$$V_{cell} = E - V_C - R_{ohm}\, I_{fcs} \tag{1}$$

I_{fcs} is the fuel cell current, V_C is the concentration voltage losses, E is the difference between the open-voltage E_0 and the transient voltage change due to the delay of fuel and oxidant E_d:

$$E = E_0 - E_d \tag{2}$$

The open-voltage E_0 is expressed through the Nernst voltage E_n as follows:

$$E_0 = 1.229 - 8.5 \times 10^{-4}\,(T_{fcs} - 298.15) + E_n \tag{3}$$

where T_{fcs} denotes the temperature of a single cell. As it was not possible to measure the exact cell temperature on the testbed, this temperature is assumed equivalent to the coolant inlet temperature $T_{fcs,in}$ for the determination of the model. This assumption has a potential impact on the accuracy of the model, as the temperature is considered uniform over the cells. The Nernst voltage E_n is obtained through the partial pressure of hydrogen at the anode catalyst interface $p_{H_2}^{ACL}$ and oxygen at cathode catalyst interface $p_{O_2}^{ACL}$:

$$E_n = \frac{R\,T}{2\,F}\, log\left(\frac{1}{p_{H_2}^{ACL}\, p_{O_2}^{CCL\,0.5}}\right) \tag{4}$$

where R and F are the universal gas constant and the Faraday constant respectively. $p_{H_2}^{ACL}$ is determined as follows:

$$p_{H_2}^{ACL} = 0.5\, p_{sat}\,(T_{fcs})\left(\frac{1}{x_{H_2O}^{ACL} - 1}\right) \tag{5}$$

where the $p_{sat}(T_{fcs})$ is the saturation pressure of water vapor in dependence of fuel cell temperature according to Vetter [47] and $x_{H_2O}^{ACL}$ is the water mole fraction at the anode catalyst interface.

The mole fractions of the reactants involved can be expressed as in Eqs. (6). These equations describe the water mole fraction from the anode channel to the catalyst interface anode $x_{H_2O}^{ACL}$, the water mole fraction in the gas channel of the anode $x_{H_2O}^{ACH}$, the water mole fraction

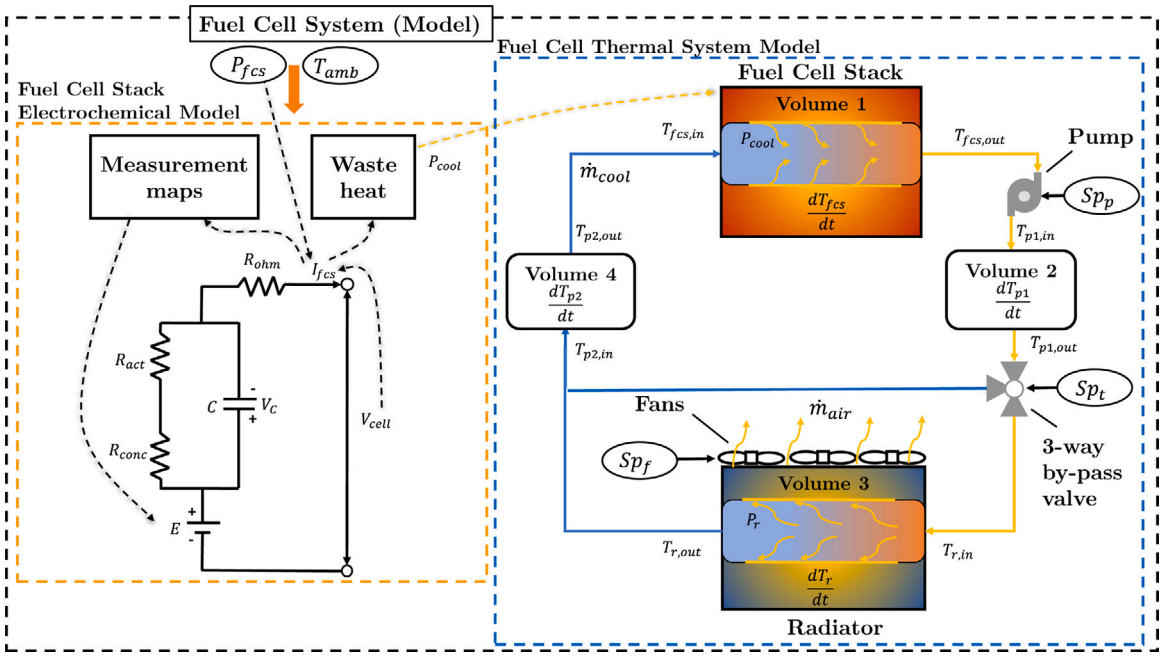

Fig. 2. Fuel cell system model obtained from testbed measurements. The model consists of a fuel cell stack electrochemical model and a thermal system model.

at the catalyst layer of the cathode $x^{CCL}_{N_2}$, the nitrogen mole fraction in the gas channel of the cathode $x^{CCH}_{N_2}$, the water mole fraction in the gas channel of the cathode $x^{CCH}_{H_2O}$:

$$x^{ACL}_{H_2O} = x^{ACH}_{H_2O}\, exp\left(\frac{R\,T_{fcs}\,I_{fcs}\,L_{ACL}\,\tau_{GDL}\,D_{H_2O\text{–}H_2}(P_a, T_{fcs})}{2\,F\,P_a\,\varepsilon_{GDL}}\right) \tag{6a}$$

$$x^{ACH}_{H_2O} = RH_a\frac{p_{sat}}{P_a} \tag{6b}$$

$$x^{CCL}_{H_2O} = x^{CCH}_{H_2O}\, exp\left(\frac{R\,T_{fcs}\,I_{fcs}\,L_{CCL}\,\tau_{GDL}\,D_{H_2O\text{–}N_2}(P_c, T_{fcs})}{4\,F\,P_c\,\varepsilon_{GDL}}\right) \tag{6c}$$

$$x^{CCL}_{N_2} = x^{CCH}_{N_2}\, exp\left(\frac{R\,T_{fcs}\,I_{fcs}\,L_{CCL}\,\tau_{GDL}\,D_{N_2\text{–}O_2}(P_c, T_{fcs})}{4\,F\,P_c\,\varepsilon_{GDL}}\right) \tag{6d}$$

$$x^{CCH}_{N_2} = 0.79\,(1 - x^{CCH}_{H_2O}) \tag{6e}$$

$$x^{CCH}_{H_2O} = RH_c\frac{p_{sat}}{p_c} \tag{6f}$$

where L_{ACL} is the length of the catalyst layer at the anode, L_{CCL} is the length of the catalyst layer at the cathode, τ_{GDL} is the diffusion transient constant in the gas diffusion layer (GDL), ε_{GDL} is the compressed GDL porosity, RH_c is the relative humidity at the cathode (assumed 1), RH_a is the relative humidity at the anode (assumed 0.75), P_c is the cathode pressure, P_a is the anode pressure, $D_{H_2O\text{–}H_2}$ is the diffusivity of water in hydrogen and $D_{H_2O\text{–}N_2}$ is the diffusivity of water in nitrogen, $D_{N_2\text{–}O_2}$ is the diffusivity of nitrogen in oxygen. The diffusivity equations are based on the work of Goshtasbi [46].

It is evident from Eqs. (6) that the anode pressure p_a and the cathode pressure p_c are necessary inputs for the model. These pressures are assumed as the average between inlet and outlet. The cathode outlet pressures $p_{c,out}$ is assumed constant and equal to the ambient pressure. The anode outlet pressure $p_{a,out}$, the anode inlet pressure $p_{a,in}$ and the cathode outlet pressure $p_{c,out}$ are determined from the measurements maps of Fig. 3 obtained from the testbed.

The gas dynamics effects on the fuel cell voltage E_d are modeled via a transfer function in Laplace domain:

$$E_d(s) = \lambda_e\, I_{fcs}\,\frac{\tau_e\, s}{\tau_e\, s + 1} \tag{7}$$

where λ_e is a constant factor expressed in Ω and τ_e is the overflow delay.

The activation voltage drop is calculated through the empirical equation of [48]:

$$V_{act} = \eta_0 + a\,T_{fcs} + T_{fcs}\,b\,ln(I_{fcs}) \tag{8}$$

where a and b are coefficients expressed in V/K and η_0 is a constant term. This equation considers the combination of two terms, where the first only depends on temperature. The second term is used for the calculation of equivalent resistance of activation losses as follows and will be used for the calculation of the double-layer charging effect:

$$R_{act} = \frac{(T_{fcs}\,b\,ln(I_{fcs}))}{I_{fcs}} \tag{9}$$

For the calculation of the ohmic resistance, the function of temperature and current is used [48]:

$$R_{ohm} = R_{ohm0} + k_{RI}\,I_{fcs} - k_{RT}\,T_{fcs} \tag{10}$$

where R_{ohm0} is the constant term, k_{RT} a coefficient for temperature dependency, k_{RI} for current dependency.

The concentration transport losses due to mass diffusions from the flow channels to the reaction sites (catalyst surfaces) is expressed based on Fick's First Law and Faraday's Law as:

$$V_{conc} = -\frac{R\,T_{fcs}}{z\,F}ln\left(1 - \frac{I_{fcs}}{I_{fcs,lim}}\right) \tag{11}$$

where z is the number of participating electrons and $I_{fcs,lim}$ is the limitation current assumed to be 450 A (based on the assumption of a current density of 1.8 A/cm^2), as measurements of the system were not possible due to the implemented controller for currents higher than 360 A. Consequently, the equivalent concentration loss resistance is given as:

$$R_{conc} = \frac{V_{conc}}{I_{fcs}} \tag{12}$$

The electrochemical double layer forms at the boundary between the porous cathode and the membrane in a fuel cell, allowing it to store electrical energy similarly to a capacitor. This occurs because electrons flow from the anode to the cathode through an external load, while protons, separated by the membrane, are drawn towards the cathode.

Table 3
Summary of fitted coefficient for the electrochemical model.

Symbol	Description	Value	Unit
a	Coefficient for temperature dependency in Eq. (8)	−0.0018	V/K
η_0	Constant in Eq. (8)	0.0901	V
b	Coefficient for temperature and currentdependency in Eq. (8)	9.16×10^{-5}	V/K
$I_{fcs,lim}$	Current limitationin Eq. (11)	450 (assumption)	A
R_{ohm0}	Constant term of ohmic losses in Eq. (10)	0.00128	Ω
k_{RT}	Temperature-dependent term of ohmic losses in Eq. (10)	3.42×10^{-6}	Ω/K
k_{RI}	Current-dependent term of ohmic losses in Eq. (10)	8.3×10^{-9}	Ω/A
τ_e	Overflow delay in Eq. (7)	4.1318	s
C	Equivalent capacitorin Eq. (13)	0.7582	F
λ_e	Constant in Eq. (7)	1.68×10^{-4}	Ω

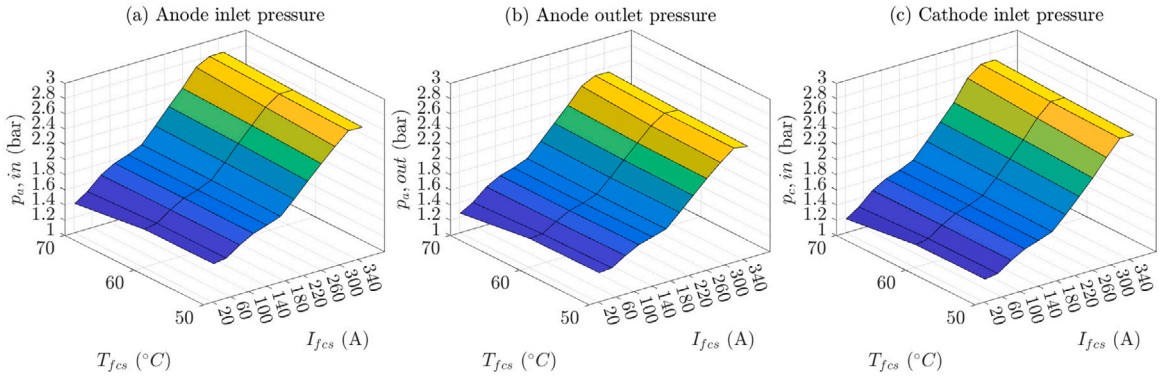

Fig. 3. Measurements maps obtained at the testbed for the determination of the anode inlet, anode outlet and cathode inlet pressure.

As in [45], the double layer effects are given by:

$$V_C = \left(I_{fcs} - C \frac{dV_C}{dt} \right) (R_{act} + R_{conc}) \tag{13}$$

where C is the equivalent capacitor due to the double-layer charging effect.

From the described equations, it is clear that several coefficients are unknown and must be defined from measurement results. Experimental data of the overall cell voltage $V_{cell,meas}$ from the testbed polarization curves (calculated from the stack voltage assuming uniformity) are deployed in a minimization problem in MATLAB [49] through particle-swarm optimization to find the coefficients that minimize this expression:

$$\min \left(\left| V_{cell,meas} - V_{\text{cell}} \right| \right) \tag{14}$$

where the model voltage is dependent on the ten coefficients: V_{cell} $\left(a, \eta_0, I_{fcs,lim}, b, R_{ohm0}, k_{RI}, k_{RT}, \tau_e, C, \lambda_e\right)$. The measurements deployed encompass three polarization curves with constant coolant inlet temperature (50, 60 and 70 °C) and one load step from 30 A to 300 A. Clearly, the amount of coefficients may result in overfitting with the given measurements. Hence, the optimization is carried out with boundaries and successive steps to keep the physical fidelity of the model. In particular, the minimization was carried out as follows:

1. a and η_0: measurement points without load (I_{fcs} equal to 0 A)
2. b, R_{ohm0}, k_{RI}, k_{RT}: polarization curve points with load
3. τ_e, C and λ_e: transient load step

As a summary, the nomenclature, unit, and values of the fitted coefficients are reported in Table 3.

The accuracy of the electrochemical model is presented in Fig. 4, where the mean absolute percentage deviation (MAPD) of the voltage cell is reported to express the model accuracy. In this work, the MAPD is defined as follows:

$$\text{MAPD} = \frac{1}{n} \sum_{i=1}^{n} \left| \frac{y_i - \hat{y}_i}{y_i} \right| \times 100 \tag{15}$$

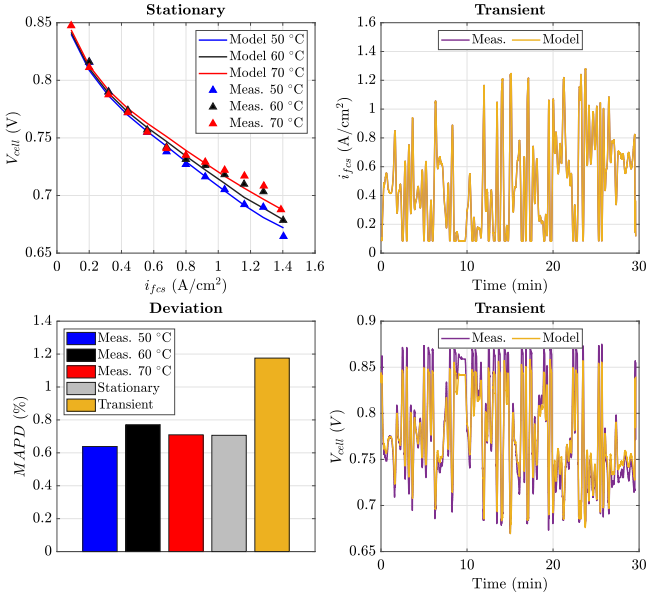

Fig. 4. Validation of the fuel cell electrochemical model against the testbed results.

where y_i is the testbed value, $\hat{y}_i$ is the modeled value, n is the total number of observations.

The left side of the graph illustrates the stationary points of the polarization curve, where the model exhibited an accuracy with a mean absolute percentage deviation (MAPD) of less than 1% compared to the measurements, as shown in the gray bar in the left bottom of Fig. 4. This accuracy is comparable to or slightly lower than the results obtained under stationary conditions in previous studies, such as [38,40], and allows the investigation of the proposed strategy under real-world conditions. The slight discrepancy may stem from the inherent limitations of the one-dimensional model in capturing the full complexity of

processes within the fuel cell stack. For instance, the model assumes a uniform cell temperature equal to the stack inlet temperature, which cannot account for the complex temperature distribution within the cell. The right side of the graph depicts a transient measurement conducted on the testbed during a simulated tractor transport cycle. In this scenario, the model continued to accurately represent the dynamic behavior of the fuel cell, achieving a MAPD of 1.2%. The slight increase in MAPD under transient conditions compared to stationary results can be attributed to two factors. First, the simplification of gas dynamics, which are modeled using a transfer function. Second, as shown in the bottom-right plot of Fig. 4, a consistent deviation is observed at low load. Since the cycles analyzed in this work primarily involve medium and high loads, the model accuracy is considered satisfactory. This result is particularly significant for accurately capturing the transient behavior of the fuel cell stack waste heat. To meet rapid power demands, the fuel cell draws more current, causing a temporary voltage undershoot. Consequently, during sudden load changes, the waste heat increases, as the higher current directly correlates with greater waste heat generation.

2.3. Fuel cell stack waste heat model and losses analysis

The electrochemical model of the stack is also used to provide valuable insights into the waste heat generation and power losses occurring within the stack. The waste heat model is formulated based on the equations governing the molar masses of hydrogen and air consumption as dictated by Faraday's law. In a fuel cell stack, the hydrogen power input $P_{\mathrm{H_2}}$ is converted into usable electric power P_{fcs} and waste heat P_{wh}. The hydrogen power input is equivalent to the hydrogen consumption $\dot{m}_{\mathrm{H_2}}$ multiplied with the lower heat value (LHV) of hydrogen $LHV_{\mathrm{H_2}}$. The waste heat in a fuel cell comprises heat removed through the coolant P_{cool} and heat expelled with the exhaust gases P_{exh}, where the latent heat of vaporization is neglected:

$$P_{\mathrm{H_2}} = P_{fcs} + P_{wh} \tag{16a}$$

$$P_{\mathrm{H_2}} = LHV_{\mathrm{H_2}}\, \dot{m}_{\mathrm{H_2}} \tag{16b}$$

$$P_{wh} = P_{cool} + P_{exh} \tag{16c}$$

The total waste heat power P_{wh} is derived from the electric power P_{fcs} and the consumption map determined from the testbed as in Fig. 5.

The waste heat in the coolant P_{cool} is evaluated by subtracting P_{exh} from P_{wh}. P_{exh} is calculated by accounting for the heat required to raise the reactants from ambient temperature to the fuel cell operating temperature:

$$P_{exh} = (c_{p,air}\, \dot{m}_{air} + c_{p,\mathrm{H_2}}\, \dot{m}_{\mathrm{H_2}})\,(T_{fcs} - T_{amb}) \tag{17}$$

where $c_{p,air}$ is the specific heat capacity of air, assumed 0.00028 kWh/(kg K), $c_{p,\mathrm{H_2}}$ is the specific heat of hydrogen, equal to 0.004 kWh/(kg K) and $\dot{m}_{air}$ is the mass flow of air. This quantity is estimated by considering the molar mass of oxygen $M_{\mathrm{O_2}}$, the molar fraction of oxygen $x_{\mathrm{O_2}}$ in air and the air stoichiometry ratio at the fuel cell inlet, $\lambda_{air,in}$:

$$\dot{m}_{air} = \frac{M_{\mathrm{O_2}}\, I_{fcs}\, \lambda_{air,in}}{4\, x_{\mathrm{O_2}}\, F} \tag{18}$$

$\lambda_{air,in}$ and $\dot{m}_{\mathrm{H_2}}$ are determined using look-up tables derived from testbed measurements, as in Fig. 5.

Fig. 6 illustrates the model's accuracy and the analysis of the waste heat generated by the fuel cell stack at 70 °C. The comparison with the polarization curve in Fig. 6a highlights the precision of the waste heat in the coolant P_{cool} with a MAPD of approximately 6%. Fig. 6b and c also depict the distribution of coolant waste heat and exhaust waste heat relative to the hydrogen power input $P_{\mathrm{H_2}}$, which are approximately 40% and 4%, respectively. Fig. 6c clearly illustrates the challenges of thermal management in a fuel cell system. At full load, approximately 100 kW of waste heat (P_{cool}) must be dissipated using the cooler, fans, and pump. Additionally, the electrochemical model facilitates the estimation of the sources of waste heat. Fig. 6d highlights the major source of waste heat and voltage losses is the open voltage losses P_{ov} with approximately 60 kW and the activation losses P_{act} with 35 kW, whereas concentration losses a P_{conc} and P_{ohm} account in total for 10 kW.

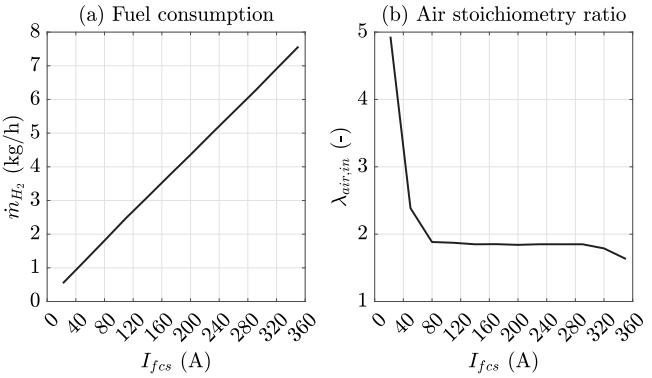

Fig. 5. Measurement maps of fuel consumption (a) and air stoichiometry ratio (b).

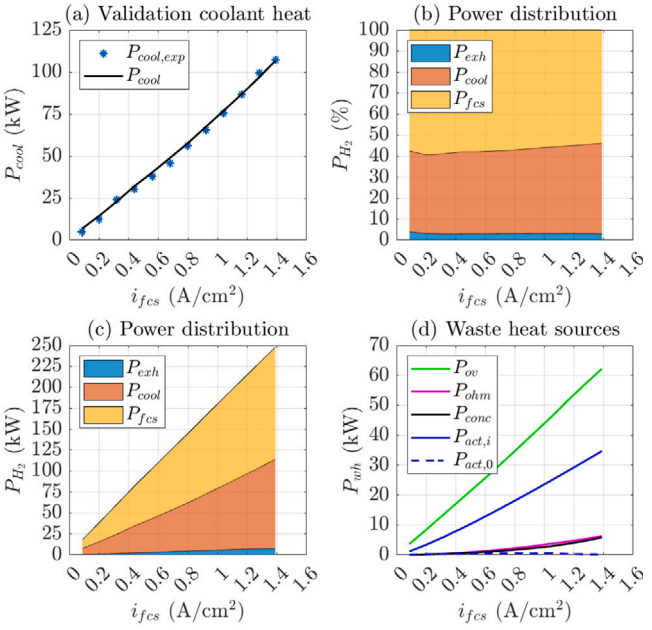

Fig. 6. Analysis of waste heat and losses of the fuel cell stack in the equivalent electric model. (a) Validation of coolant waste heat with polarization curve at 70 °C. (b) Power distribution of input hydrogen. (c) Percentage power distribution of input hydrogen. (d) Sources of losses and waste heat from electrochemical model.

2.4. Thermal system model

A four-volume thermal system model, as illustrated in Fig. 2, is deployed in this work as a non-linear plant model to accurately depict the stack inlet and outlet temperature for the given waste heat and actuator action. The four volumes correspond to the main components of the thermal system: fuel cell stack, radiator and two pipes in-between. Moreover, the thermal system is equipped with one three-way by-pass valve, one coolant pump and six fans on the radiator. This model is used to estimate the temperature of coolant circuit given ambient temperature, coolant waste heat, fans and pump setpoints.

Table 4
Summary of parameters used for the thermal system model.

Component	Description	Value	Unit
Fuel cell stack	Weight	77	kg
	Specific heat cap.	752.5	J/(kg K)
	Convective heat transfer coeff.	1	W/(K m^2)
	Channels number	80	–
	Channel length	300	mm
	Channel diameter	0.5	mm
Pump	Max. flow	5.2	kg/s
	Max. power	1.2	kW
Fans	Max. flow	4.8	kg/s
	Max. rate	12	%/s
	Max. power	3.3	kW
Radiator	Channels rows	83	–
	Channels layers	4	–
	Channel length	1.1	m
	Channel width	2	mm
	Channel height	20	mm
	Convective heat transfer area	19.72	m^2
	Convective heat transfer coeff.	70	W/(K m^2)
Pipe 1 and 2	Diameter	50	mm
	Length	2	m
	Weight	0.583	kg
	Specific heat cap.	1300	J/(kg K)

The model is implemented as a non-linear model through SIMSCAPE in MATLAB with the relevant parameters shown in Table 4. The thermal system utilizes approximately 35 l of 50/50 mixture of glycol and deionized water as the coolant with an electric conductivity lower than 3 μS/cm. This low value is necessitated by the coolant's direct contact with high voltage within the bipolar plates. The specific heat capacity of the coolant $c_{p,cool}$ at 60 °C is approximately 3450 J/(kg K). The thermal inertia of the coolant significantly impacts the system's dynamics, with the coolant being distributed across different volumes as follows: 13 l in the fuel cell, 6 l in the pipes, and 16 l in the radiator. It is essential to note that in this study, the HV cooling circuit of the HV BoP components is not modeled, under the assumption that the operating points of these components, specifically the air compressor and hydrogen recirculation blower, remain constant, as the electric load of the fuel cell is not varied. Furthermore, the model does not incorporate the 3-way bypass valve because its primary function is to rapidly increase temperature during the warm-up phase. This study focuses on optimizing the cooling performance of the thermal system during medium and high load cycles when the 3-way bypass valve is fully opened and it is therefore omitted.

The fuel cell stack is modeled as a single coolant channel of the bipolar plates in order to keep the physical behavior for heat transfer. The mass flow of the single channel is successively multiplied by the number of channels in the plate n_{chann}, which is assumed to be 80, and the number of cells equal n_{cell} to 560. The heat transfer in the single channel is parametrized based on the Dittus-Boelter correlation:

$$Nu = 0.1\, Re^{0.8}\, Pr^{0.4} \tag{19}$$

The temperature of the fuel cell stack T_{fcs} is calculated based on the energy equilibrium of the single channel. Assuming uniform partition of weight, area and mass flow throughout the channels, the energy equilibrium of the single channel to the stack energy equilibrium expressed as:

$$\begin{aligned} m_{fcs}\, c_{p,fcs}\, \dot{T}_{fcs} = {} & \dot{m}_{cool}\, c_{p,fcs}\, (T_{fcs,out} - T_{fcs,in}) \\ & - K_{fcs}\, A_{fcs}\, (T_{fcs} - T_{amb}) + P_{cool} \end{aligned} \tag{20}$$

where the dry stack weight is 77 kg. The specific heat capacity of the stack $c_{p,fcs}$ is a decisive factor for the temperature dynamics and is considered to be 752.5 J/(kg K) with the assumption of the following weight distribution [50] and material composition [51] at 60 °C: 90% graphite from the bipolar plates, current collectors and end plates, 5% tetrafluoroethylene from the membrane, 5% silicone from the sealings. The convective heat transfer is modeled through the coefficient K_{fcs}, equal to 1 W/(K m^2), and the heat exchange area A_{fcs}, assumed to be the sum of each channel area with diameter d_{chann} and length l_{chann}, respectively 0.5 mm and 300 mm.

The primary actuators in the thermal system are the pump and the six radiator fans, and they are driven by the setpoint: Sp_p for the pump and Sp_f for the fans. These auxiliary components operate in a coordinated manner to cool the fuel cell stack and are modeled based on the curves of Fig. 7a and b. The pump has a maximum rated mass flow of 5.2 kg/s and a maximum power consumption of 1.2 kW. The power consumption P_p and mass flow rate curves $\dot{m}_p$ for the pump are presented in Fig. 7a. The asterisk points in the graph indicate the experimental values measured at the testbed. The six fans are mounted on the radiator, collectively providing a maximum mass flow of 4.8 kg/s with a maximum power consumption of 3.3 kW. At the testbed, a transient characteristic of approximately 8 s was observed for a setpoint change from 0 to 100%. Hence, a maximum rate of 12%/s was implemented in the model. The performance curves for the fans are shown in Fig. 7b. Due to the inability to measure the mass flow accurately at the testbed, the curve depicts the values provided in the manufacturer's datasheet.

The radiator is modeled as a heat exchanger, where the specific dissipation ξ of Fig. 7c is used to calculate the heat transfer. The radiator's geometry consists of 83 channel rows arranged over four layers. Each channel measures approximately 1.1 m in length, 2 mm in width, and 20 mm in height. This geometry is simplified to a prismatic shape, resulting in a natural convective heat transfer area A_r of 19.7 m^2. The total heat exchange area is estimated to be 39.4 m^2, assuming the fin surface area is equal to that of the channels. The convective heat transfer coefficient h_r, estimated from measurements, is 24 W/(K m^2). The specific dissipation ξ is the coefficient that governs the heat transfer in the model and was determined by fitting experimental results from the testbed. Specifically, a fitting dataset of 16 operating points at an ambient temperature of 23 °C with various combinations of inputs was used to fit the resulting temperatures of the model. The fitting process achieved a mean absolute deviation of 2.3 °C for the inlet temperature and 1.2 °C for the outlet temperature with the fitting dataset. The waste heat that is removed by the radiator P_r is given by:

$$P_r = \xi\, (T_{r,out} - T_{r,in}) + h_r\, A_r\, (T_r - T_{amb}) \tag{21}$$

where the natural convective heat transfer model is deactivated when the forced convective heat transfer of the fans is active. The radiator is made of aluminum, with a specific heat capacity at 60 °C of 897 J/(kg K) and a mass m_r of 94 kg.

The two pipes connecting the radiator and fuel cell stack are assumed as entirely made of silicone and modeled as two separate volumes with a specific heat capacity $c_{p,p}$ of 1300 J/(kg K). The length and diameter of each volume are assumed to be 2 m and 50 mm, respectively, with a weight m_p of 0.583 kg.

2.5. Overall model validation

The accuracy of the modeled fuel cell stack temperatures is evaluated by comparing them with experimental results from a validation dataset, using identical input parameters: fuel cell stack power P_{fcs}, ambient temperature T_{amb}, pump setpoint Sp_p, and fan setpoint Sp_f. This evaluation was conducted under both steady-state and transient conditions. The steady-state analysis involved 21 operating points with varying input combinations, including ambient temperatures ranging from 20 to 40 °C, fuel cell stack powers from 50 to 95 kW, and fan and pump setpoints between 10% and 100%. The comparison yields an absolute mean deviation of 3.2 °C for the inlet temperature and 2.7 °C for the outlet temperature in a range of temperatures between 45 °C and 75 °C. It must be noted the validation dataset presents a higher deviation from the training dataset mainly because of the

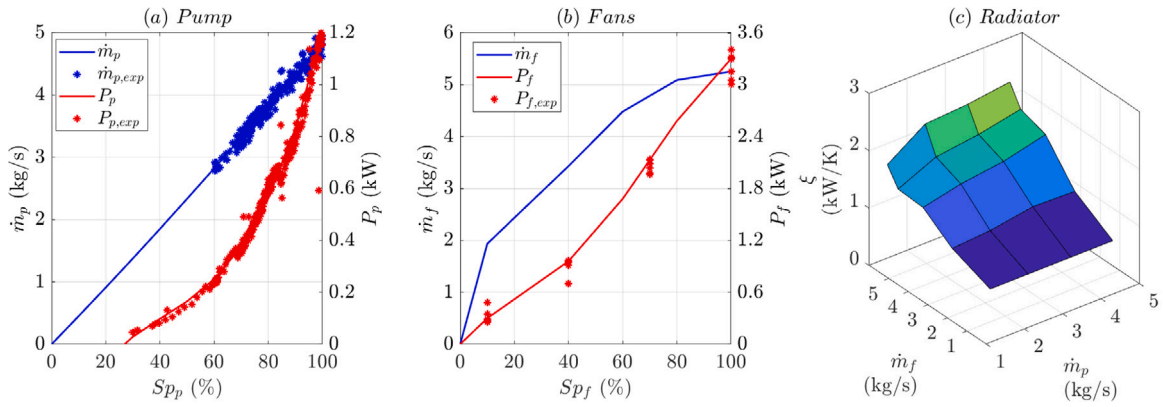

Fig. 7. Implemented parameters for the thermal system model. Pump mass flow and consumption (a), fans mass flow and consumption (b), and radiator specific dissipation (c).

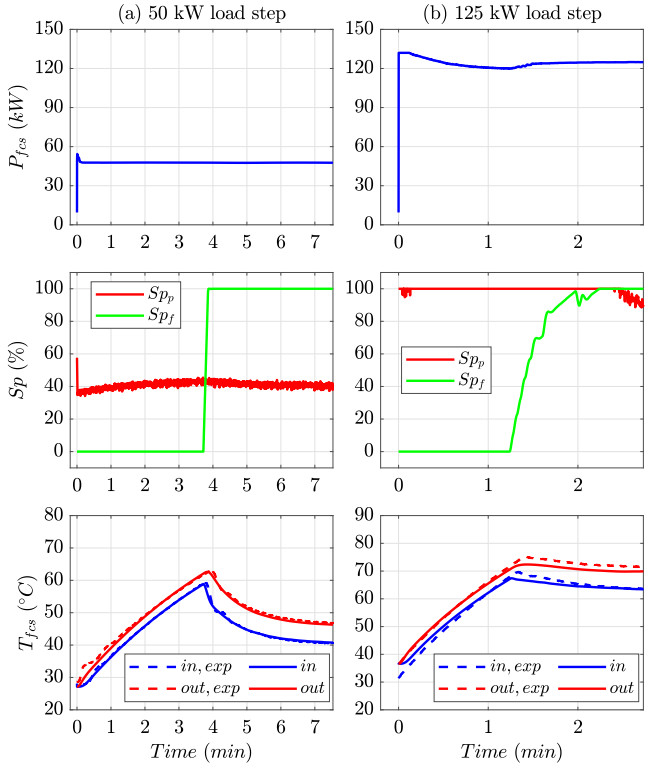

Fig. 8. Overall validation of the thermal system model. The figure depicts a 50 kW load step (a) and a 125 kW load step (b) that are carried out in the model with the same relevant inputs: ambient temperature, fuel cell stack power, and pump and fans setpoint. The lowest graphs show the resulting temperature of the fuel cell stack against the experimental values.

larger range of the ambient temperature. Furthermore, the model was validated using transient measurements conducted with two fuel cell stack power load steps, as illustrated in Fig. 8. The measured power load steps of 50 kW and 125 kW, along with the setpoints for the fans and pump, were used as inputs for the model. The comparison of the temperatures in Fig. 8 demonstrates the model's high accuracy under transient conditions. Specifically, for the 50 kW load step, the mean absolute deviation of the inlet and outlet temperatures is 0.3 °C and 0.7 °C, respectively. For the 125 kW load step, these values are 1.1 °C and 1.3 °C. The high accuracy under transient conditions supports the development of advanced control strategies, such as MPC, which can forecast future behavior and optimize performance in real-time. Leveraging the model dynamic predictions, MPC can adjust parameters to reduce the auxiliaries energy consumption and maintain the reference setpoints.

It should be noted that the temperature graph in Fig. 8 also underscores the high inertia of the cooling circuit. This inertia is attributed to the substantial mass of the system, particularly the fuel cell stack and the volume of coolant, as well as the reaction time of the fans, which is approximately 8 s from 0 to 100%. This significant system inertia can be effectively compensated by predictive control, as will be discussed in Section 3.

3. Fuel cell thermal system control

This section presents the strategies investigated for controlling the thermal system. As a summary, the control goals of the fuel cell stack thermal system are to maintain a constant coolant inlet temperature $T_{fcs,insp}$ of 60 °C and to track a reference coolant temperature difference between the outlet and inlet $\Delta T_{fcs,sp}$, which varies between 3 and 12 °C based on the drawn current from the stack. The fuel cell system is cooled using two types of actuators: a coolant pump and six fans mounted on the radiator, with control variables denoted as Sp_p for the pump and Sp_f for the fans. In this study, a classical control approach implemented in the fuel cell system is compared against an MPC strategy. The objective of the MPC TMS is to deploy information to optimize control precision and energy consumption. As demonstrated in Section 4, the MPC approach effectively compensates for the system's inherent inertia by utilizing a control model and minimizes power losses through the solution of a minimization problem. In this study, the fuel cell system model, measured at the testbed, is used as the plant model for the simulations.

3.1. Requirements and classical control of thermal system

In the fuel cell thermal system, the pump and fans are employed to dissipate the waste heat generated by the stack. This requirement is managed through the control of the stack temperature, a critical factor that significantly influences both the degradation and efficiency of the fuel cell. Achieving a delicate balance between these two competing objectives typically involves measurements specific to the fuel cell stack, which are then translated into a reference value for the controller to maintain. Since the stack temperature is not directly measured, the inlet and outlet temperatures of the fuel cell are used as control variables. This study considers the reference temperatures that are already implemented in the controller. The first reference is a constant coolant inlet temperature $T_{fcs,insp}$ set at 60 °C. The second reference is a dynamic value representing the temperature difference $\Delta T_{fcs,sp}$, as illustrated in Fig. 9. This dynamic reference is chosen to limit temperature gradients within the stack, thereby reducing degradation at low current levels, while a larger temperature difference at high

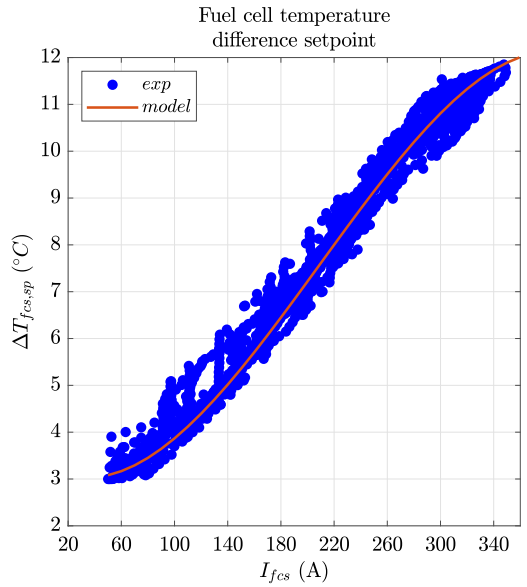

Fig. 9. The fuel cell temperature difference setpoint implemented in the controller and the corresponding model through a polynomial.

current levels reduces actuator losses by increasing the temperature differential between the radiator and the ambient air, thus enhancing heat exchange.

The classical control structure implemented in the thermal system is depicted in Fig. 10, where a dedicated controller is designed for each reference signal. The fan controller outputs the fans setpoint Sp_f and employs a PI-controller with the stack coolant inlet temperature difference between the setpoint as its input. The integral coefficient, $K_{i,f}$, is set to 2 to ensure appropriate convergence behavior. The proportional coefficient, $K_{p,f}$, is designed to limit overshoot during transient response to below 70 °C and is set to 30 with a model execution time of 10 ms. The pump controller uses the stack coolant temperature difference as its input. Given that the pump controller's action is closely linked to the fan controller, its dynamics are deliberately constrained to prevent instabilities. Accordingly, the proportional and integral coefficients, $K_{p,p}$ and $K_{i,p}$, are set to 2 and 4, respectively. To achieve a responsive dynamic behavior, a feedforward controller based on the drawn current I_{fcs} is incorporated. This addition does not introduce instabilities to the fan controller. The parameters for this controller are derived from experimental results of three current load steps, as shown in Fig. 11. It is evident from these results that the pump setpoint Sp_p is closely dependent on the fuel cell stack current I_{fcs}, as the setpoint in Fig. 11b remains constant when the current in Fig. 11a is steady. The observed behavior is modeled using a fitted look-up table, as illustrated in Fig. 11c.

The analysis of the thermal system controller highlights the robust and real-time implementation of the fuel cell controller. However, it is evident the classical control approach has the following drawbacks when deployed for thermal management:

1. A separate controller is assigned to each reference signal. Given the physical coupling between the inlet and outlet temperatures, controlling these two temperatures simultaneously may lead to instabilities. Therefore, one of the controllers must be carefully designed with dynamic limitations, which may result in a less precise tracking of the reference temperature.
2. No real-time optimization is employed. The traditional thermal system controller consists of both closed-loop and open-loop controllers, which are parameterized offline based on specific measurements and may not generalize various conditions of the control problem. Consequently, this approach can lead to suboptimal use of actuators and an increase in auxiliary power losses.
3. No predictive strategies are employed. In classical control, closed-loop controllers determine the appropriate actuator setpoint based solely on the deviation from the given reference. Due to the high inertia of the thermal system, this deviation may result in a delayed signal, leading to less precise tracking of the reference temperatures and potentially compromising the timely control of the system.

To solve these drawbacks of classical control, an MPC approach for the fuel cell thermal system is discussed in Section 3.3 and benchmarked in Section 4. The analysis in 3.2 examines the benchmarking cycles and explores the potential of utilizing forecast predictions in agricultural operations.

3.2. Optimizing agricultural duty cycles: leveraging forecast prediction in farming operations

In this study, the realistic cycles developed by the Deutsche Landwirtschafts-Gesellschaft (DLG, German Agricultural Society) are considered, as these cycles serve as the benchmark for tractor performance evaluation in German-speaking countries [52]. The individual test cycles simulate typical scenarios of field and transport applications at both half load and full load, where the tractor engages in pure drawbar work (e.g., cultivating or plowing) as well as mixed work involving load from the power-take-off (PTO) and the hydraulic system [53]. To streamline the analysis and focus on key operational scenarios for tractors, the cycles Z1G, Z5K, and Z7PR are selected due to their distinct profiles and characteristic loads. A detailed analysis of the electric load associated with these cycles can be found in [44]. In summary, cycle Z1G is characterized by a high load (approximately 85 kW on average), Z5K by a low load (approximately 42 kW on average), and Z7PR by a dynamically varying intermediate load (approximately 70 kW on average). The fuel cell power demand in [44], determined by the load-following energy management strategy, serves as the input for the fuel cell model in this study. Furthermore, the repetitive nature of agricultural tasks suggests that future electric loads can be anticipated based on these recurring patterns. The electric load typically peaks in the central regions of the field where agricultural tasks are actively performed, while it decreases at the headlands where the implements are disengaged. Hence, a model can be implemented to predict the future electric load based on the current operational conditions, such as position on the field, implements engagement and current power. The information on future load fluctuations can be effectively utilized to forecast the load of upcoming operational scenarios. As demonstrated in [19], machine learning techniques for operational pattern recognition during agricultural cycles have the potential to enhance energy management strategies for fuel cell electric tractors, enabling near-optimal solutions to be achieved. Therefore, predictive forecasting can facilitate the adoption of electrified agricultural machinery by enabling the implementation of advanced predictive strategies. These control frameworks can reduce the energy consumption of electrified and sustainable powertrains, enhancing both the economic and environmental benefits.

3.3. Model predictive control of thermal system

This study proposes a nonlinear MPC to manage the actuators of the fuel cell thermal system. The detailed formulation of an MPC can be found in [54–56]. In summary, MPC involves the successive online optimization of the input control sequence u_{k+1} over a defined control horizon N_c within a prediction horizon N_p, while considering the optimization criteria and constraints. From this optimized sequence, only the first input sample $u^*(k)$ is implemented as the control command.

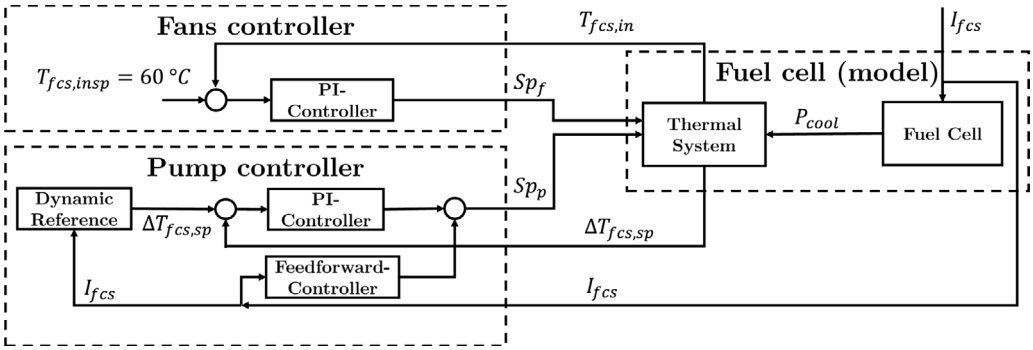

Fig. 10. Structure of classical control implemented in the fuel cell system controller.

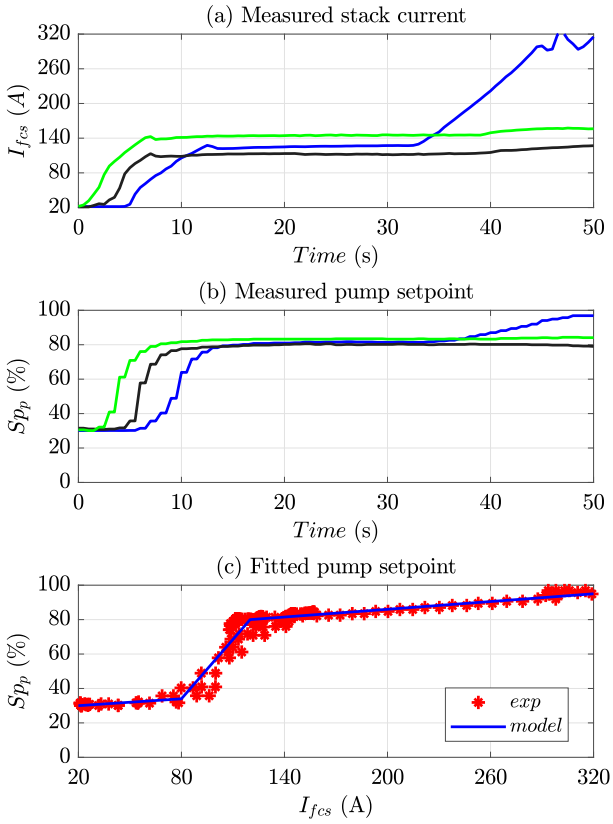

Fig. 11. Measured current (a), measured pump setpoint (b), and fitted pump setpoint (c) for three given load steps.

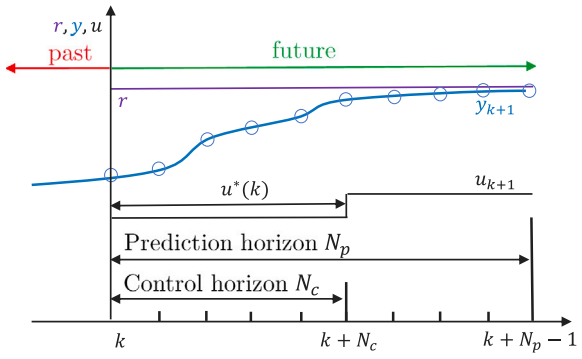

Fig. 12. Basic principle of MPC.
Source: Adapted from [54].

The basic principle is illustrated in Fig. 12.

The key aspect of non-linear MPC lies in utilizing a non-linear control-oriented model to optimize the system's performance based on predicted disturbances and the reference trajectory to be tracked. The analysis of the fuel cell system of Section 2 highlights the thermal system is a nonlinear multi-input multi-output system. To enable fast real-time optimization, the control-oriented model is further abstracted by excluding the thermostat and focusing solely on coolant temperatures, as these are the primary variables to be controlled. Additionally, the transient effects of fuel cell stack waste heat are neglected, with waste heat instead represented through a look-up table. Given the simple flow setup, the equations for mass conservation are straightforward to derive. Starting from the first law of thermodynamics for open systems, we assume constant volumes with no accumulation of mass or energy. Additionally, changes in potential and kinetic energy, as well as internal energy variations due to pressure changes, are neglected, and it is assumed that no work is being performed. Moreover, each component temperature is assumed to be equal to the coolant outlet temperature of the corresponding component, as depicted in Fig. 13. For further abstraction of the analysis, the temperature dependence of the heat capacity is disregarded, and the specific heat capacity of the coolant $c_{p,c}$ is assumed to be constant. The model parameters are taken from Section 2. For the sake of simplicity, it is assumed natural convective heat transfer only takes place in the radiator and the thermal inertia of the coolant is concentrated in the radiator. The equations for the four volumes can then be expressed in the following compact and discrete form:

$$T_{p_1}(k+1) = \frac{c_{p,cool}\,\dot{m}_{cool}(k)\,(T_{fcs}(k) - T_{p_1}(k))}{c_{p,p}\,m_p + 0.2\,c_{p,cool}\,m_{cool}} \tag{22a}$$

$$T_{fcs}(k+1) = \frac{c_{p,cool}\,\dot{m}_{cool}(k)\,(T_{p_2}(k) - T_{fcs}(k)) + P_{cool}(k)}{c_{p,fcs}\,m_{fcs} + 0.1\,c_{p,cool}\,m_{cool}} \tag{22b}$$

$$T_{p_2}(k+1) = \frac{c_{p,cool}\,\dot{m}_{cool}(k)\,(T_r(k) - T_{p_2}(k))}{c_{p,p}\,m_p + 0.2\,c_{p,cool}\,m_{cool}} \tag{22c}$$

$$T_r(k+1) = \frac{c_{p,cool}\,\dot{m}_{cool}(k)\,(T_{p_1}(k) - T_r(k)) - P_r(k)}{c_{p,r}\,m_r + 0.5\,c_{p,cool}\,m_{cool}} \tag{22d}$$

In these equations, the selected sample time T_s of the MPC strategy is one second, and therefore omitted in the formulation. The waste heat dissipated by the radiator, P_r, is defined as in Eq. (21). Despite the simplifications, the model is non-linear. The accuracy of the control-oriented model is crucial for predicting future states and optimizing the performance of the MPC. To better align the plant model with the control-oriented model, the original dissipation factor ξ is modified accordingly, and the natural convective heat transfer coefficient h_r is set to 10 W/(K m^2). For the load cycles presented in Section 4 at 20 °C, the control-oriented model exhibited a mean absolute deviation of 0.8 °C for the fuel cell outlet temperature and 0.7 °C for the inlet temperature compared to the plant model, given the same initial conditions and actuator setpoints over the entire cycle. At 40 °C, the mean

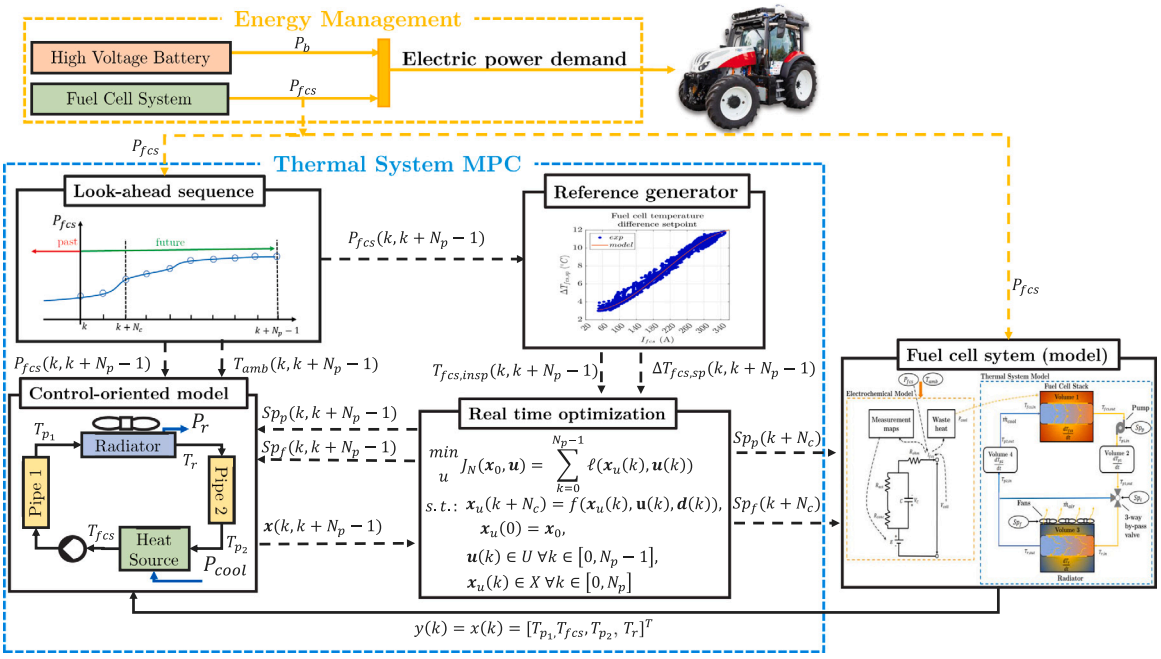

Fig. 13. Structure of the fuel cell thermal system MPC.

absolute deviation is 0.7 °C and 0.6 °C. It is important to note that this deviation represents a minimal difference, as the predicted states are calculated within the limited interval of the prediction horizon, with the current states being updated based on the actual temperatures of the plant model. The mathematical model of Eq. (22) can be rewritten in the general form describing dynamic systems governed by ordinary differential equations in discrete time:

$$\mathbf{x}(k+1) = f(\mathbf{x}(k), \mathbf{u}(k), \mathbf{d}(k)) \tag{23a}$$

$$\mathbf{y}(k) = \mathbf{x}(k) \tag{23b}$$

$$\mathbf{x}_0 = \mathbf{x}(0) \tag{23c}$$

where f is a non-linear function, $\mathbf{x}(k) = [T_{p_1}, T_{fcs}, T_{p_2}, T_r]^T$ is the state vector, $\mathbf{u}(k) = [Sp_p, Sp_f]^T$ is the control vector, and $\mathbf{d}(k) = [T_{amb}, P_{fcs}]^T$ is the vector of the measured disturbances. The selected sample time T_s of the MPC strategy is one second, as the system's dynamics are slow and do not require a fast sampling rate. Additionally, a longer sample time helps to prevent strong oscillations. A control horizon N_c of two seconds has been chosen. The MPC formulation considers a running stage cost function to track the given reference:

$$l(\mathbf{x}, \mathbf{u}) = \|x_u - x^r\|_Q^2 + \|u - u^r\|_R^2 \tag{24}$$

where $x^r = [0, T_{fcs} + \Delta T_{fcs,sp}, T_{fcs,insp}, 0]$ are the reference setpoints illustrated in Section 3.1, x_u is the predicted reference for the given control inputs, Q and R are respectively the weight matrix for the reference and control vectors. The weights in the cost function are selected to achieve a balance between two objectives: tracking accuracy and actuator cost reduction. These weights are defined as follows:

$$Q = \begin{pmatrix} 0 & 0 & 0 & 0 \\ 0 & Q_1 & 0 & 0 \\ 0 & 0 & Q_2 & 0 \\ 0 & 0 & 0 & 0 \end{pmatrix}, \quad R = \begin{pmatrix} R_1 & 0 \\ 0 & R_2 \end{pmatrix} \tag{25}$$

It is important to note that in Q, the weights Q_1 and Q_2 are assigned based on the specific prediction horizon. Assigning higher values to the matrix Q for the reference control compared to the matrix Q for the control vector would result in a control strategy that prioritizes reference tracking performance over the reduction of actuator energy consumption. The matrix R plays a critical role in coordinating the pump and fan actuation. Specifically, assigning a higher value to the fan weight R_2 than the pump weight R_1 would lead to a thermal management control strategy that minimizes fan actuation more. In this study, given the higher energy consumption of the fans, the fan weight R_2 is given a higher weight than the pump weight R_1. The weights are found as a trade-off between reference tracking and energy consumption under the considered agricultural cycles and their effect is discussed further in the results of Section 4.4. In addition to the reference and control input cost functions, there are cost functions to consider constraints to limit control inputs within feasible values. The limits of Sp_p and Sp_f are respectively [30, 100]% and [0, 100]% and the rate limits are [−100, 50]%/s and [−25, 12]%/s. The selection of weights in an MPC framework is tailored to a specific model and its corresponding operating conditions. These weights can be thought of as degrees of freedom for the designer to prioritize the considered performance criteria and are a critical aspect of tuning MPC to achieve the desired performance for a given control model and plant model configuration within the prescribed boundary conditions. The performance of the MPC when applying the same weights to a different model largely depends on the degree of similarity between the two models and the context of the application. If the models share comparable dynamic behaviors, the weights originally designed for one model may yield satisfactory performance for the other. This is because MPC inherently performs an online optimization to minimize the specified cost function, adapting to the system dynamics within the given constraints. However, significant differences in the dynamics of operating conditions between the models could necessitate the re-tuning of the weights to maintain optimal performance. These significant differences may emerge when the model is applied to scenarios that differ substantially from those for which it was originally developed. To address these considerations, this work examines various operating conditions and weight configurations, demonstrating the effectiveness of the proposed strategy. Furthermore, regularization functions are added to the cost function to improve system stability when small reference deviations are present, which are often caused by discrepancies between the control model and the plant model. This is done by penalizing deviations from the current actuator setpoint in proportion to the temperature

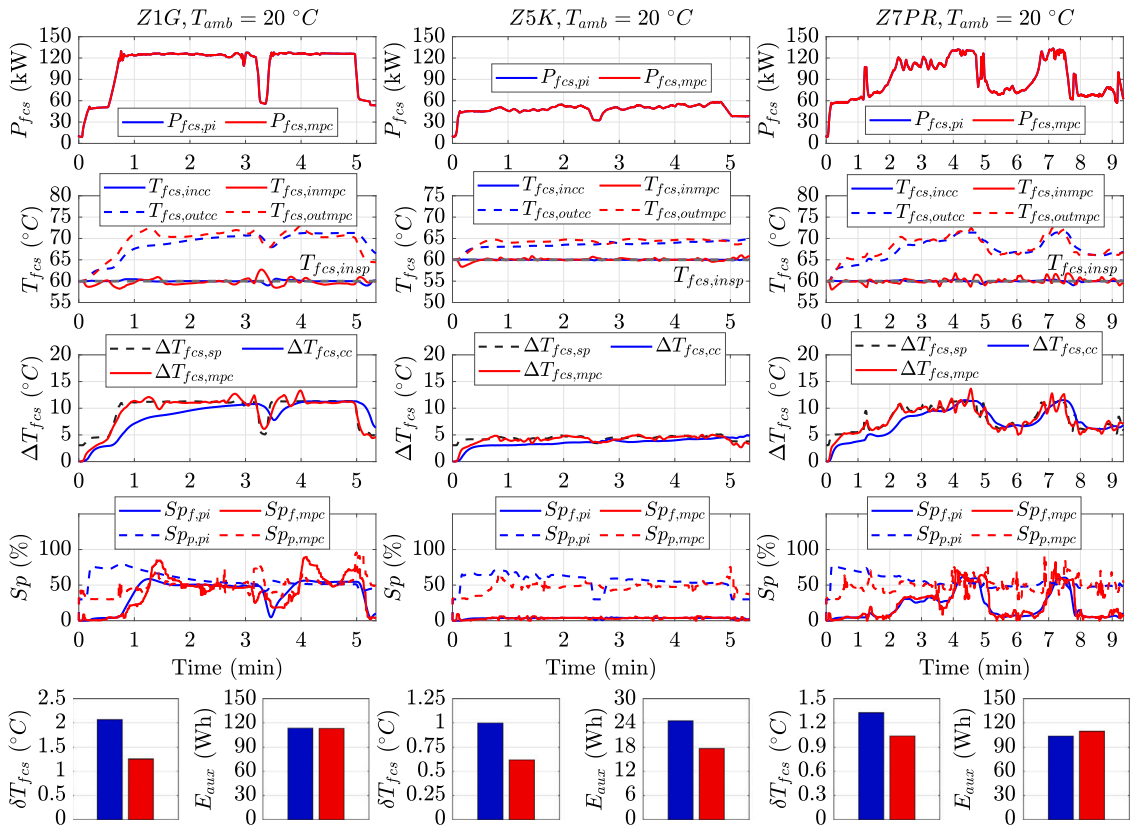

Fig. 14. Results of the proposed MPC (red) against classical control (CC) TMS (blue) for cycles Z1G, Z5K, and Z7PR, respectively left, middle, and right column, at the ambient temperature of 20 °C. The considered strategy is denoted with the subscript CC or MPC. The first row from the top reports the fuel cell electric load P_{fcs}. The second row depicts the fuel cell stack coolant temperature inlet $T_{fcs,in}$ and outlet $T_{fcs,in}$. The fuel cell stack inlet is shown with $T_{fcs,in}$. The third row from the top display the fuel cell stack coolant difference and its setpoint $\Delta T_{fcs,sp}$. The fourth row depicts the setpoint of the pump Sp_p and of the fan Sp_f. The bar graphs in the bottom row report the quantification of the performance with the parameters δT_{fcs}, representing the sum of the mean absolute deviations between the temperature setpoints at both the stack coolant inlet and outlet and the actuators consumption E_{aux}.

reference deviation, thereby improving tracking for deviations smaller than the model's accuracy. Without this adjustment, the original cost function would cause sudden changes in actuator activity, leading to instabilities and control process discontinuities during minimal reference deviations.

The optimal control problem consists of finding a minimizing control sequence u for the evaluation of the running costs over the prediction horizon N_p subject to the constraints:

$$\begin{aligned} \min_{u} \quad & J_{N_c}(\mathbf{x},\mathbf{u}) = \sum_{k=0}^{N_p-1} l(\mathbf{x}_u(k),\mathbf{u}(k)) \\ \text{s.t.} \quad & \mathbf{x}_u(k+1) = \mathbf{f}(\mathbf{x}_u(k),\mathbf{u}(k),\mathbf{d}(k)), \\ & \mathbf{x}_u(0) = \mathbf{x}_0, \\ & \mathbf{u}(k) \in U, \forall k \in [0, N_p], \\ & \mathbf{x}_u(k) \in X, \forall k \in [0, N_p] \end{aligned} \tag{26}$$

In this study, the influence of the prediction horizon is examined by varying it between 5 and 55 s, in increments of 10 s.

The implementation of the MPC controller is conducted using CasADi [57], an open-source tool designed for nonlinear optimization. In CasADi, the previous non-linear MPC problem and its corresponding control-oriented equations are constructed as symbolic expressions with MATLAB functions. The optimal control problem defined in Eq. (26) is solved by CasADi using shooting methods and is transcribed into a nonlinear programming problem with an objective function Φ and equality constraints g:

$$\begin{aligned} \min_{w} \quad & \Phi_w \\ \text{s.t.} \quad & g(w) = 0, \quad w \in W \end{aligned} \tag{27}$$

where w represents the control variable and W denotes the corresponding interval set. In this study, a multiple shooting method was employed to enhance computational efficiency and mitigate the increase in computation time as the prediction horizon expands.

4. Results

This section demonstrates the effectiveness of MPC in a model-based environment, using the complex plant model validated with testbed measurements as the real system. This approach aims at simulating potential deviations between the control model and the real plant, as would occur in the real system. The MPC controller is compared to classical control (CC) methods of Section 3.1 using realistic cycles at ambient temperatures of 20 °C and 40 °C, in order to evaluate the impact of ambient temperature on both controller performance and the thermal system's energy consumption, with a prediction horizon of 35 s. The selection of this specific prediction horizon is further justified by an analysis of its influence on controller performance and computation time across different temperature levels and agricultural cycles. Furthermore, an analysis of the actuator weights in the cost function is carried out to highlight the balance between reference tracking and auxiliary consumption. Following this, the MPC controller with the 35-s prediction horizon is examined in greater detail to assess the influence of forecast accuracy on the control performance and to determine the requirements for an electric load predictor.

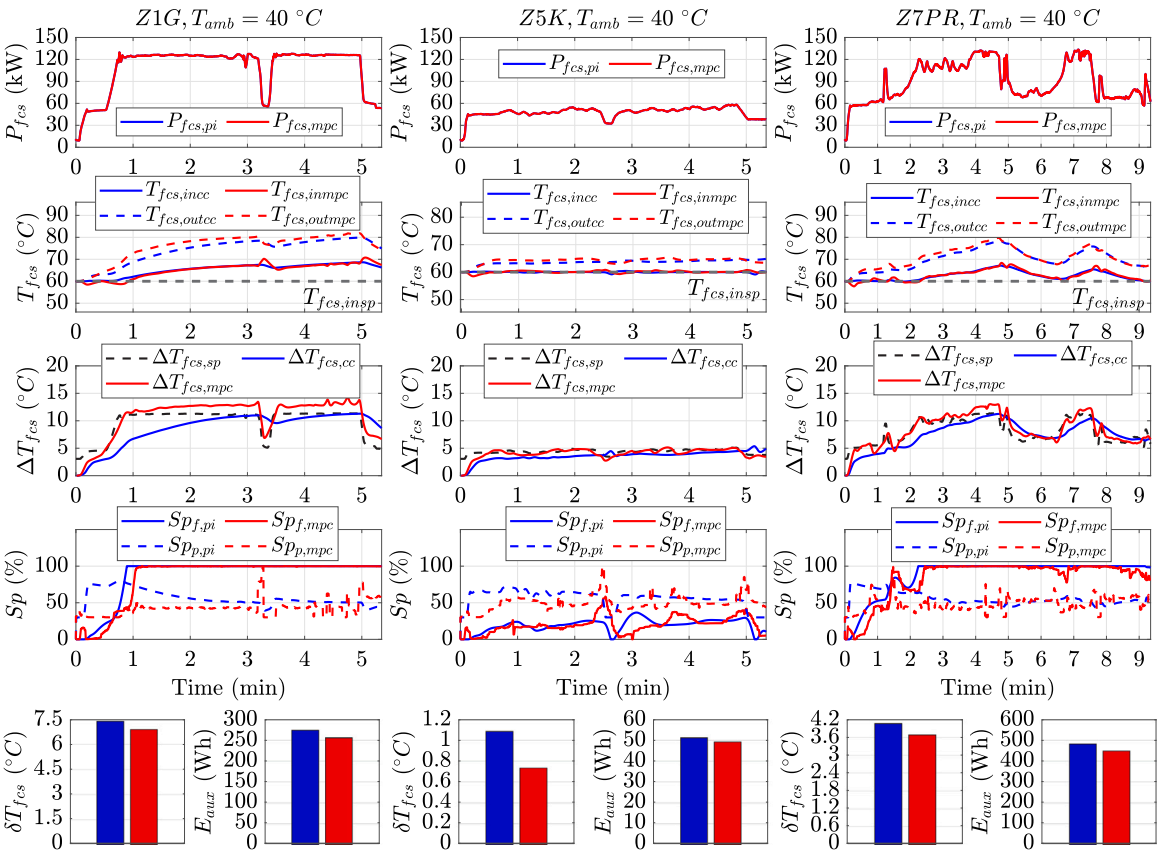

Fig. 15. Results of the proposed MPC TMS (red) against classical control TMS (blue) for cycles Z1G, Z5K, and Z7PR, respectively left, middle, and right column, at the ambient temperature of 40 °C. The considered strategy is denoted with the subscript CC or MPC. The first row from the top reports the fuel cell electric load P_{fcs}. The second row depicts the fuel cell stack coolant temperature inlet $T_{fcs,in}$ and outlet $T_{fcs,in}$. The fuel cell stack inlet is shown with $T_{fcs,in}$. The third row from the top display the fuel cell stack coolant difference and its setpoint $\Delta T_{fcs,sp}$. The fourth row depicts the setpoint of the pump Sp_p and of the fan Sp_f. The bar graphs in the bottom row report the quantification of the performance with the parameters δT_{fcs}, representing the sum of the mean absolute deviations between the temperature setpoints at both the stack coolant inlet and outlet and the actuators consumption E_{aux}.

4.1. Comparison of MPC with classical control strategies

The results obtained at an ambient temperature of 20 °C and a 35-s prediction horizon are presented in Fig. 14. The first row shows the fuel cell stack power P_{fcs}, the second and third rows represent the control states to be tracked, respectively the stack coolant temperatures T_{fcs} and the coolant temperature difference $\Delta T_{fcs,sp}$. The fourth row displays the control variable of the actuators: the pump setpoint Sp_p and the fans setpoint Sp_f. The bar plots at the bottom of Fig. 14 visualize the control performance with the introduction of two parameters: the parameter δT_{fcs}, representing the sum of the mean absolute deviations between the temperature setpoints at both the stack coolant inlet and outlet and the actuators consumption E_{aux}. δT_{fcs} is calculated as follows:

$$\delta T_{fcs} = \frac{1}{n}\sum_{i=1}^{n}\left|T^i_{fcs,in} - T^i_{fcs,insp}\right| + \left|\Delta T^i_{fcs} - \Delta T^i_{fcs,sp}\right| \tag{28}$$

where n is the number of points in the cycle. The percentage variation of δT_{fcs} between MPC and CC is calculated as follows:

$$\frac{\delta T_{fcs,mpc} - \delta T_{fcs,cc}}{\delta T_{fcs,cc}} \times 100 \tag{29}$$

where a negative value indicates a reduction of temperature deviation of MPC compared to CC. Similarly, the percentage deviation of auxiliary consumption (pump and fans) E_{aux} is indicated as:

$$\frac{E_{aux,mpc} - E_{aux,cc}}{E_{aux,cc}} \times 100 \tag{30}$$

where a negative value indicates a reduction of consumption of MPC compared to CC.

For the MPC control algorithm, the selected weights, Q_1 and Q_2, are 2.25 and 0.975, respectively, prioritizing the tracking of the fuel cell outlet temperature, $T_{fcs,outsp}$, which serves as a dynamic reference. The actuator weights R_1 and R_2 are 10^{-9} and 4×10^{-4} to favor a lower usage of fans and, therefore, lower auxiliary consumption. In the second and third row, where the stack temperatures are shown, it is evident that while the CC method ensures stable but sluggish temperature tracking during load changes, the proposed MPC TMS delivers a more responsive performance without major instabilities. In CC TMS, given that the pump controller's action is closely linked to the fan controller, its dynamics are deliberately constrained to prevent instabilities, as depicted in a stable tracking of the inlet temperature in the second row and a sluggish tracking of the temperature difference in the third row. On the contrary, the MPC method favors tracking both setpoints equally based on the cost function formulation, resulting in a better tracking $\Delta T_{fcs,sp}$ at the expense of the inlet temperature, $T_{fcs,insp}$, compared to the traditional control strategy. This effect is particularly pronounced in the third row of Z7PR cycle, where the MPC successfully tracks the complex dynamic reference profile under varying loads.

4.2. Performance under different agricultural duty cycles

The advantages of predictive control are notably visible in Fig. 14 during load changes, especially in cycle Z1G, where the pump setpoint is adjusted in advance to address the low temperature difference $\Delta T_{fcs,sp}$ at the change from high loads to low loads at the middle (3.2 min) and at the end of the cycle (5.1 min). The excellent tracking performance of the fuel cell outlet temperature results in a higher

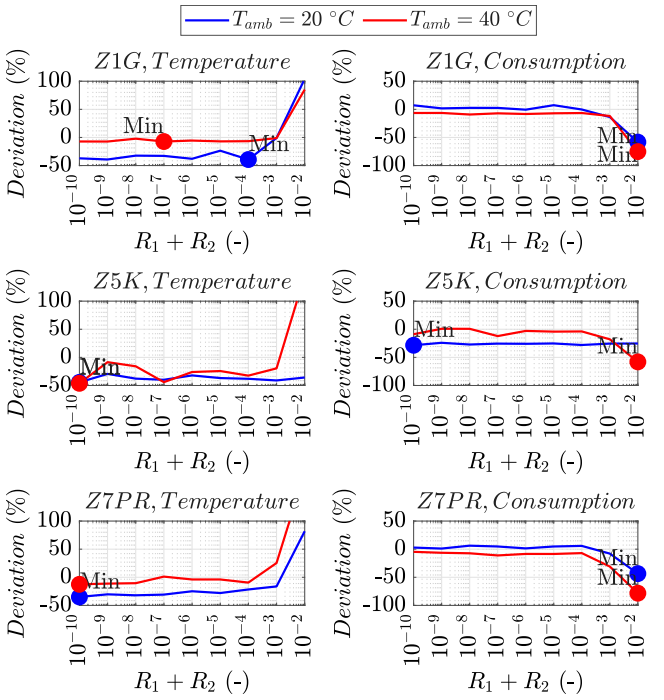

Fig. 16. Variation of actuator cost weights R_1 and R_2 for the comparison of percentage deviation of temperature setpoints and auxiliary consumption between the CC TMS and MPC TMS is compared. A negative percentage deviation represents a lower deviation and consumption of MPC compared to CC and a zero percentage deviation depicts the same performance for both strategies.

temperature at high load, which favors heat exchange with less fan consumption. Furthermore, the Z1G cycle provides valuable insights into the performance of the MPC controller compared to CC. Analyzing the sum of the temperature mean absolute deviations, δT_{fcs}, in Fig. 14 reveals higher reference tracking for MPC, with a value of 1.2 °C, compared to 2 °C for CC. Since the first half of the Z1G cycle resembles a load step, it also offers information about the response time. The results indicate that MPC achieves a response time of approximately 1 min, whereas CC is three times slower. Overall, the MPC approach yields a lower mean absolute deviation in tracking the reference compared to CC, achieving a significant reduction of 39%, 38%, and 22% for cycles Z1G, Z5K, and Z7PR, respectively, without a major increase of auxiliary consumption E_{aux}, which includes the power usage of both the fans and the pump. In the Z5K cycle, a 30% reduction in auxiliary consumption is observed. It should be noted that cycle Z7PR exhibits an increase of 6%, attributed to the dynamic nature of the cycle, which demands greater control effort for a reduction of the temperature deviation δT_{fcs}.

The results obtained at an ambient temperature of 40 °C and a 35-s prediction horizon are illustrated in Fig. 15, showing more benefits than previously observed at 20 °C. Notably, the MPC approach demonstrates a lower mean absolute deviation in tracking the reference, achieving significant reductions of 7%, 33%, and 9% alongside a decrease in auxiliary consumption (E_{aux}) of 6%, 4%, and 7%, for cycles Z1G, Z5K, and Z7PR, respectively, compared to CC.

4.3. Impact of ambient temperature on auxiliary consumption

Table 5 reports the consumption for each cycle at 20 °C and 40 °C. The comparison between MPC and CC at 40 °C highlights the consistently lower auxiliary consumption of MPC across all cycles. For instance, in the Z1G cycle, MPC consumes 256 Wh compared to 274 Wh with CC. For both controllers, the increase in ambient temperature from 20 °C to 40 °C leads to an average rise of approximately three times, reflecting the additional energy demand of the actuators on the fuel cell system from mild to extreme weather conditions.

Table 5
Comparison of the results at 20 °C and 40 °C.

Cycle/Control	E_{aux} at 20 °C	E_{aux} at 40 °C
Z1G/CC	113 Wh	274 Wh
Z1G/MPC	113 Wh	256 Wh
Z5K/CC	25 Wh	51 Wh
Z5K/MPC	18 Wh	49 Wh
Z7PR/CC	103 Wh	482 Wh
Z7PR/MPC	109 Wh	448 Wh
Average	80 Wh	260 Wh

4.4. Variation of actuators cost function weights

The effect of varying the actuator cost function weights is shown in Fig. 16, where the percentage deviation of temperature setpoints and auxiliary consumption between the CC TMS and MPC TMS is compared on the y-axis. These parameters indicate the performance of the MPC compared to the traditional strategy. Specifically, a negative percentage deviation represents a lower deviation and consumption of MPC compared to CC, and a zero percentage deviation depicts the same performance for both strategies. The analysis considers the sum of the weights, with higher values making actuator use more costly, at the expense of precise temperature control. This is particularly evident in cycles Z7PR and Z5K, where the smallest temperature deviation occurs at the lowest weight sum, $R_1 + R_2$. As the weights increase, actuator usage becomes more efficient, leading to reduced auxiliary consumption (E_{aux}). However, temperature control performance deteriorates for weight sums above 10^{-3}, especially at 40 °C ambient temperature, where actuator use is highest. The optimal weight sum, where performance is minimized for every cycle temperature and consumption deviation, is around 10^{-4}, and it was used in the analyses in Section 4.1.

4.5. Variation of prediction horizon

The impact of the prediction horizon length is depicted in Fig. 17, which shows the percentage deviation in temperature setpoint differences and auxiliary consumption between the CC and MPC approaches. It must be noted the prediction horizon has a large effect on the cost function formulation, and therefore, the weights have been modified to achieve comparable performance. The analysis indicates that temperature deviations mostly reach an optimal solution for prediction horizons between 15 s and 35 s, with a saturating trend for long prediction horizons due to the increase of the inaccuracy of the control-oriented model in the MPC. Auxiliary consumption deviations exhibit a similar saturating trend, with minima occurring primarily between 45 s and 55 s. The sporadic minima at 5 s suggest that, while auxiliary consumption is lowest, temperature control performance is poor. The average prediction horizon at which the minima are achieved is 35 s, whose results are extensively discussed in Section 4.1.

The length of the prediction horizon is a critical parameter affecting computation time, as extending the prediction horizon increases the size of the optimization vector. The impact of the prediction horizon on the simulation time is provided as an indication for assessing the real-time capability of the MPC strategy in Fig. 18, where the percentage simulation time difference between CC and MPC for the cycle Z1G at 20 °C for different prediction horizons is depicted. Here, the computation time is defined as the time to carry out the cycle simulation. It should be noted that this time is highly dependent on the specific optimization problem, particularly the solver and its configuration, the computational power of the system, and the formulation of the cost function. The solver employed is an interior-point filter line-search algorithm for large-scale nonlinear programming (“ipopt”) [58], with a maximum of 100 iterations. Fig. 18 illustrates that the simulation time is between 40% and 170% higher than that of the traditional control strategy, depending on the chosen prediction horizon. The fact that the MPC’s computation time is only marginally higher suggests

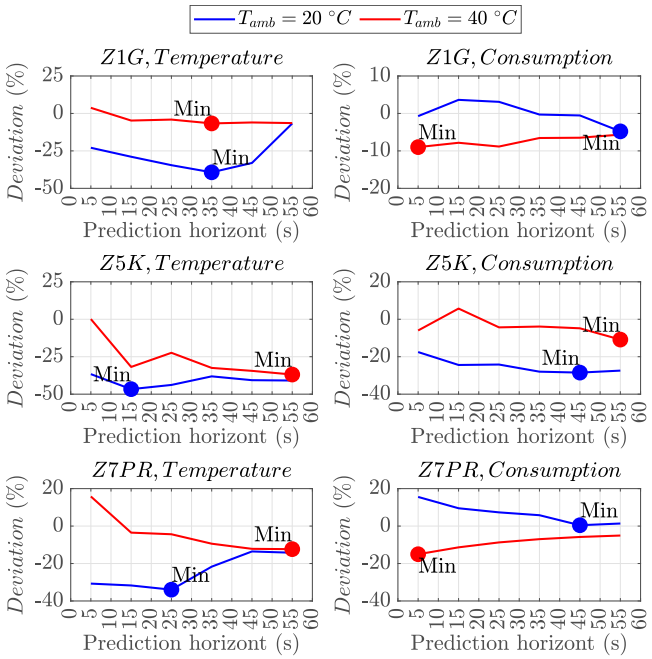

Fig. 17. Analysis of prediction horizon length variation and its effect on the performance of the MPC TMS, showing the percentage deviation in temperature setpoint differences and auxiliary consumption between the CC and MPC approaches. A negative percentage deviation represents a lower deviation and consumption of MPC compared to CC and a zero percentage deviation depicts the same performance for both strategies.

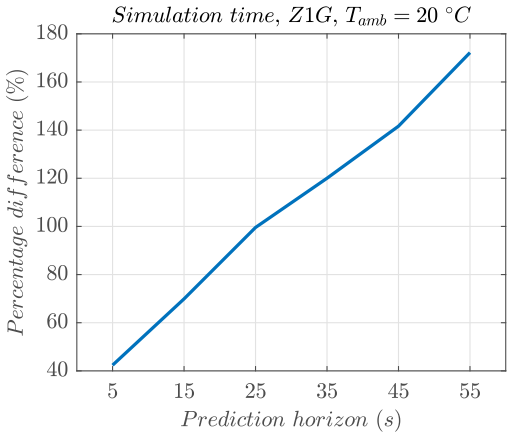

Fig. 18. Analysis of prediction horizon length variation and its effect on simulation time of MPC TMS computation in comparison with the CC TMS.

that it can still operate within real-time constraints on suitable hardware, demonstrating its potential for deployment in real-world systems without significant performance degradation.

Table 6 summarizes the results of the prediction horizon variation for cycle Z1G at 20 °C in terms of computation time, temperature variation, and energy consumption. It is important to note that the values for the CC strategy remain constant across the prediction horizons, as the traditional strategy is unaffected by these variations.

4.6. Effect of prediction accuracy

The performance of the MPC TMS is evaluated by introducing noise into the fuel cell power prediction P_{fcs}, in order to assess the requirements for an accurate load prediction model. The noise is added to the measured disturbance vector of fuel cell power prediction and it is modeled as a combination of exponential magnitude and white

Table 6
Summary of prediction horizon variation for the cycle Z1G at 20 °C.

Prediction horizon (s)	5	15	25	35	45	55
CC, computation time (s)	62	62	62	62	62	62
MPC, computation time (s)	89	106	125	137	151	170
CC, δT_{fcs} (°C)	2.1	2.1	2.1	2.1	2.1	2.1
MPC, δT_{fcs} (°C)	1.6	1.5	1.4	1.3	1.4	1.9
CC, E_{aux} (kW)	0.113	0.113	0.113	0.113	0.113	0.113
MPC, E_{aux} (kW)	0.113	0.118	0.117	0.113	0.113	0.108

Gaussian noise as follows:

$$P_{fcs,err}(k, k+N_p-1) = P_{fcs}(k, k+N_p-1) + exp(\alpha(k, k+N_p-1))\, N(0, \sigma^2, k) \tag{31}$$

The factor α is the growth rate of the exponential magnitude and represents an increase of prediction inaccuracy over the prediction horizon, which is assumed equal to 1.6. The function N represents a normally Gaussian distributed time-based variation of accuracy and is considered equal for the entire exponential vector. The Gaussian distribution has 0 mean and its variance σ is varied between 0 and 2×10^6 to represent a less accurate fuel cell power prediction. It must be noted the noisy fuel cell power prediction is capped between the minimum and maximum power of the fuel cell stack. The root-mean-square error (RMSE) between the noiseless and noisy predictions is used as the x-axis in Fig. 19.

The analysis reveals that the load cycles Z7PR and Z1G at 40 °C exhibit greater susceptibility to accuracy variations, as the performance benefits of the MPC are minimal under these conditions. Specifically, for cycle Z7PR, MPC performance falls below that of the CC TMS, with an RMSE of 50 kW observed at 20 °C. This decline is evident in the third row of the left column, where the temperature deviation between the CC and MPC increases, indicating less accurate tracking of the fuel cell coolant temperatures by the MPC. Notably, the performance degradation of MPC is more pronounced for cycles Z1G and Z7PR at 40 °C, with RMSE values around 10 kW. Conversely, the low load cycle Z5K and the high load cycle Z1G at 20 °C show greater resilience to prediction inaccuracies, with significant performance degradation occurring only when RMSE exceeds 50 kW. Additionally, the right column shows a slight increase in auxiliary consumption deviation, which reflects an overall degradation in MPC controller performance. Overall, this investigation underscores the robustness of the MPC TMS for every cycle and temperature for RMSE under 10 kW. This points out the effectiveness of the proposed strategy even in the presence of substantial prediction inaccuracies, while also highlighting the requirements for an effective load prediction model to ensure optimal MPC performance.

5. Conclusion

This paper introduces a novel predictive thermal management strategy for the fuel cell systems of agricultural tractors. A model predictive control approach is proposed to tackle the substantial inertia of heavy-duty fuel cells while optimizing actuator utilization by integrating a control-oriented model with real-time predictions. The unique contribution is to employ a comprehensive methodology, beginning with an extensive non-linear model of the 132-kW fuel cell system derived

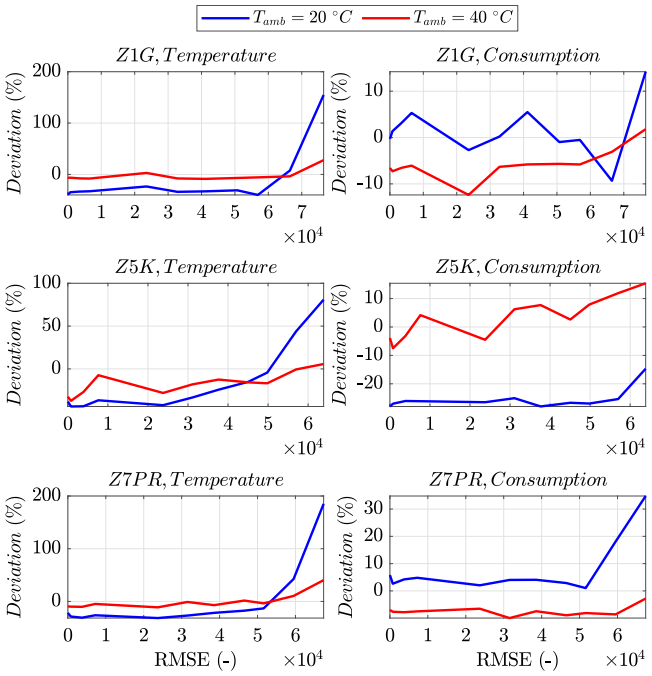

Fig. 19. Analysis of prediction horizon accuracy variation and its effect on MPC performance. The left column depicts the temperature deviation between CC and MPC, and the right column indicates the auxiliary consumption deviation. The analysis is performed for cycles Z1G, Z5K, and Z7PR at 20 °C and 40 °C. A negative percentage deviation represents a lower deviation and consumption of MPC compared to CC and a zero percentage deviation depicts the same performance for both strategies.

from experimental measurements that highlight the electrochemical characteristics of the stack, substantial thermal system inertia, and waste heat amount. Cooling is facilitated by larger radiators and fans, which exhibit significant inertia. Existing feedback-based controllers typically rely on deviations from the prescribed inlet temperature, potentially resulting in delayed responses.

The proposed model predictive control thermal management strategy demonstrates the advantages of incorporating load change predictions. By effectively combining actuator actions into a single cost function, the strategy enhances temperature control and reduces auxiliary consumption. Specifically, at low loads, reference tracking performance improves by up to 38%, while auxiliary consumption decreases by up to 30% compared to classical control strategies across various ambient temperatures. As a unique aspect of this study, the broad analysis identifies key parameters for optimizing model predictive control, including cost function weights, prediction horizon, and prediction accuracy. The appropriate selection of prediction horizon and cost weights for actuator actions balances auxiliary consumption and temperature tracking. Furthermore, the evaluation of prediction accuracy underscores the robustness of the controller under noisy predictions and the requirements for an electric load prediction model to ensure the effective performance of the model predictive control. Overall, the comprehensive investigation in this study demonstrates the benefits and robustness of deploying predictive thermal management for heavy-duty fuel cells, showing reduced auxiliary demands and improved controller performance compared to state-of-the-art methods through the inclusion of a model-based optimization problem.

Future research could focus on validating the proposed strategies in real-world applications across diverse agricultural scenarios and varying ambient conditions. Additionally, exploring cost-effective hardware solutions for real-time implementation of model-predictive control in agricultural machinery remains a crucial area of interest. A promising direction would be the development of advanced prediction techniques, such as machine learning-based load forecasting, specifically tailored to agricultural tractors. These forecast-driven strategies could further enhance thermal management control while reducing auxiliary consumption. Furthermore, integrating additional actuators or subsystems, such as bypass valves, into the model-predictive control framework represents a valuable avenue for exploration. Finally, integrating thermal management with health-aware energy management strategies is strongly recommended to minimize overall powertrain consumption and extend the fuel cell's operational lifetime.

Declaration of competing interest

The authors declare that they have no known competing financial interests or personal relationships that could have appeared to influence the work reported in this paper.

Acknowledgments

This project is supported with funds from the Climate and Energy Fund, Austria and implemented in line with the "Zero Emission Mobility" program. The computational results presented were achieved using the Vienna Scientific Cluster (VSC). The authors acknowledge TU Wien Bibliothek for financial support through its Open Access Funding Program.

Data availability

The data that has been used is confidential.

References

[1] The sustainable development goals report 2021, Sustain. Dev. Goals Rep. (2021) URL https://api.semanticscholar.org/CorpusID:242208799.

[2] H.H. Vogt, R.R. de Melo, S. Daher, B. Schmuelling, F.L.M. Antunes, P.A. dos Santos, D. Albiero, Electric tractor system for family farming: Increased autonomy and economic feasibility for an energy transition, J. Energy Storage 40 (2021) 102744, http://dx.doi.org/10.1016/j.est.2021.102744, URL https://www.sciencedirect.com/science/article/pii/S2352152X21004497.

[3] R. Hagan, E. Markey, J. Clancy, M. Keating, A. Donnelly, D.J. O'Connor, L. Morrison, E.J. McGillicuddy, Non-road mobile machinery emissions and regulations: A review, Air 1 (1) (2023) 14–36, http://dx.doi.org/10.3390/air1010002, URL https://www.mdpi.com/2813-4168/1/1/2.

[4] E. Scolaro, M. Beligoj, M.P. Estevez, L. Alberti, M. Renzi, M. Mattetti, Electrification of agricultural machinery: A review, IEEE Access 9 (2021) 164520–164541, http://dx.doi.org/10.1109/ACCESS.2021.3135037.

[5] A. Ghobadpour, L. Boulon, H. Mousazadeh, A.S. Malvajerdi, S. Rafiee, State of the art of autonomous agricultural off-road vehicles driven by renewable energy systems, Energy Procedia 162 (2019) 4–13, http://dx.doi.org/10.1016/j.egypro.2019.04.002, URL https://www.sciencedirect.com/science/article/pii/S187661021931361X, Emerging and Renewable Energy: Generation and Automation.

[6] A. Trukhanov, S. Trukhanov, L. Panina, V. Kostishyn, I. Kazakevich, A. Trukhanov, E. Trukhanova, V. Natarov, V. Turchenko, M. Salem, A. Balagurov, Evolution of structure and magnetic properties for bafe11.9al0.1o19 hexaferrite in a wide temperature range, J. Magn. Magn. Mater. 426 (2017) 487–496, http://dx.doi.org/10.1016/j.jmmm.2016.10.140, URL https://www.sciencedirect.com/science/article/pii/S0304885316328104.

[7] Y. Yao, V. Zhivulin, A. Zykova, N. Cherkasova, D. Vinnik, E. Trofimov, S. Gudkova, O. Zaitseva, S. Taskaev, L. Alyabyeva, B. Gorshunov, A. Gurchenko, S. Lu, S. Trukhanov, A. Trukhanov, High entropy BaFe12-x(Ti/Mn/Ga/In)xo19 (x=1–7) oxides: Correlation of the composition, entropy state, magnetic characteristics, and terahertz properties, Ceram. Int. 49 (19) (2023) 31549–31558, http://dx.doi.org/10.1016/j.ceramint.2023.07.106, URL https://www.sciencedirect.com/science/article/pii/S0272884223020321.

[8] J.K. Winkler, A. Grahle, A.M. Syré, K. Martins-Turner, D. Göhlich, Fuel cell drive for urban freight transport in comparison to diesel and battery electric drives: a case study of the food retailing industry in berlin, Eur. Transp. Res. Rev. 14 (2022) 1–14, URL https://api.semanticscholar.org/CorpusID:246493023.

[9] C. Lorenzo, D. Bouquain, S. Hibon, D. Hissel, Synthesis of degradation mechanisms and of their impacts on degradation rates on proton-exchange membrane fuel cells and lithium-ion nickel–manganese–cobalt batteries in hybrid transport applications, Reliab. Eng. Syst. Saf. 212 (2021) 107369, http://dx.doi.org/10.1016/j.ress.2020.107369, URL https://www.sciencedirect.com/science/article/pii/S0951832020308589.

[10] P. Ren, P. Pei, Y. Li, Z. Wu, D. Chen, S. Huang, Degradation mechanisms of proton exchange membrane fuel cell under typical automotive operating conditions, Prog. Energy Combust. Sci. 80 (2020) 100859, http://dx.doi.org/10.1016/j.pecs.2020.100859, URL https://www.sciencedirect.com/science/article/pii/S0360128520300691.

[11] M. Moein-Jahromi, M. Kermani, S. Movahed, Degradation forecast for PEMFC cathode-catalysts under cyclic loads, J. Power Sources 359 (2017) 611–625, http://dx.doi.org/10.1016/j.jpowsour.2017.05.102, URL https://www.sciencedirect.com/science/article/pii/S037877531730753X.

[12] J. Höflinger, P. Hofmann, B. Geringer, Experimental PEM-Fuel Cell Range Extender System Operation and Parameter Influence Analysis, Tech. Rep., SAE Technical Paper, 2019.

[13] Z. Song, Y. Pan, H. Chen, T. Zhang, Effects of temperature on the performance of fuel cell hybrid electric vehicles: A review, Appl. Energy 302 (2021) 117572, http://dx.doi.org/10.1016/j.apenergy.2021.117572, URL https://www.sciencedirect.com/science/article/pii/S0306261921009508.

[14] Q. Chen, G. Zhang, X. Zhang, C. Sun, K. Jiao, Y. Wang, Thermal management of polymer electrolyte membrane fuel cells: A review of cooling methods, material properties, and durability, Appl. Energy 286 (2021) 116496, http://dx.doi.org/10.1016/j.apenergy.2021.116496, URL https://www.sciencedirect.com/science/article/pii/S030626192100057X.

[15] H. Boodaghi, M.M. Etghani, K. Sedighi, Performance analysis of a dual-loop bottoming organic rankine cycle (ORC) for waste heat recovery of a heavy-duty diesel engine, part I: Thermodynamic analysis, Energy Convers. Manage. 241 (2021) 113830, http://dx.doi.org/10.1016/j.enconman.2021.113830, URL https://www.sciencedirect.com/science/article/pii/S0196890421000078.

[16] J. Hoeflinger, J. Konrad, C. Steindl, A.-O. Bernt, A. Schaerfl, P. Hofmann, Thermal design of a system for mobile hydrogen powersupply, Appl. Therm. Eng. 237 (2024) 121718, http://dx.doi.org/10.1016/j.applthermaleng.2023.121718, URL https://www.sciencedirect.com/science/article/pii/S1359431123017477.

[17] G. Zhang, S.G. Kandlikar, A critical review of cooling techniques in proton exchange membrane fuel cell stacks, Int. J. Hydrog. Energy 37 (3) (2012) 2412–2429, http://dx.doi.org/10.1016/j.ijhydene.2011.11.010, URL https://www.sciencedirect.com/science/article/pii/S0360319911024980, 2010 AIChE Annual Meeting Topical Conference on Hydrogen Production and Storage Special Issue.

[18] V. Gubin, C. Varlese, F. Benedikt, J. Konrad, S. Müller, D.C. Rosenfeld, P. Hofmann, FCTRAC and BioH2Modul–a way to zero emission mobility in agriculture, in: International Conference on Drives and Energy Systems of Tomorrow, Springer, 2022, pp. 86–104.

[19] C. Varlese, P. Hofmann, C. Junger, J. Konrad, R. Krizan, D. Brunner, C. Mayer, K. Masser, FCTRAC fuel cell tractor: Operating strategy for real-duty scenarios, in: 45th International Vienna Motor Symposium, 2024, http://dx.doi.org/10.62626/9cdw-cugb.

[20] M. Mattetti, M. Maraldi, N. Lenzini, S. Fiorati, E. Sereni, G. Molari, Outlining the mission profile of agricultural tractors through CAN-BUS data analytics, Comput. Electron. Agric. 184 (2021) 106078, http://dx.doi.org/10.1016/j.compag.2021.106078, URL https://www.sciencedirect.com/science/article/pii/S016816992100096X.

[21] A.P. Vega-Leal, F.R. Palomo, F. Barragán, C. García, J.J. Brey, Design of control systems for portable PEM fuel cells, J. Power Sources 169 (1) (2007) 194–197, http://dx.doi.org/10.1016/j.jpowsour.2007.01.055, URL https://www.sciencedirect.com/science/article/pii/S0378775307002273, CONAPPICE 2006.

[22] D. O'Keefe, M. El-Sharkh, J.C. Telotte, S. Palanki, Temperature dynamics and control of a water-cooled fuel cell stack, J. Power Sources 256 (2014) 470–478, http://dx.doi.org/10.1016/j.jpowsour.2013.12.100, URL https://www.sciencedirect.com/science/article/pii/S0378775313020892.

[23] J. Höflinger, P. Hofmann, Thermal management of a fuel cell range-extended electric vehicle, in: J. Liebl (Ed.), Der Antrieb Von Morgen 2017, Springer Fachmedien Wiesbaden, Wiesbaden, 2017, pp. 121–138.

[24] J. Han, J. Park, S. Yu, Control strategy of cooling system for the optimization of parasitic power of automotive fuel cell system, Int. J. Hydrog. Energy 40 (39) (2015) 13549–13557, http://dx.doi.org/10.1016/j.ijhydene.2015.08.067, URL https://www.sciencedirect.com/science/article/pii/S0360319915021965.

[25] V. Liso, M.P. Nielsen, S.K. Kær, H.H. Mortensen, Thermal modeling and temperature control of a PEM fuel cell system for forklift applications, Int. J. Hydrog. Energy 39 (16) (2014) 8410–8420, http://dx.doi.org/10.1016/j.ijhydene.2014.03.175, URL https://www.sciencedirect.com/science/article/pii/S0360319914008672.

[26] P. Hu, G.-Y. Cao, X.-J. Zhu, M. Hu, Coolant circuit modeling and temperature fuzzy control of proton exchange membrane fuel cells, Int. J. Hydrog. Energy 35 (17) (2010) 9110–9123, http://dx.doi.org/10.1016/j.ijhydene.2010.06.046, URL https://www.sciencedirect.com/science/article/pii/S036031991001222X.

[27] C.-Q. Su, J.-F. Sun, G.-D. Meng, X. Liu, Y.-P. Wang, Thermal management control strategy of liquid-cooled fuel cell vehicle, Energy Rep. 8 (2022) 141–153, http://dx.doi.org/10.1016/j.egyr.2022.10.235, URL https://www.sciencedirect.com/science/article/pii/S2352484722021722, Selected papers from 2022 7th International Conference on Advances on Clean Energy Research.

[28] Y.-X. Wang, F.-F. Qin, K. Ou, Y.-B. Kim, Temperature control for a polymer electrolyte membrane fuel cell by using fuzzy rule, IEEE Trans. Energy Convers. 31 (2) (2016) 667–675, http://dx.doi.org/10.1109/TEC.2015.2511155.

[29] J. Han, S. Yu, S. Yi, Advanced thermal management of automotive fuel cells using a model reference adaptive control algorithm, Int. J. Hydrog. Energy 42 (7) (2017) 4328–4341, http://dx.doi.org/10.1016/j.ijhydene.2016.10.134, URL https://www.sciencedirect.com/science/article/pii/S0360319916332281.

[30] S.-R. Oh, J. Sun, H. Dobbs, J. King, Model predictive control for power and thermal management of an integrated solid oxide fuel cell and turbocharger system, IEEE Trans. Control Syst. Technol. 22 (3) (2014) 911–920, http://dx.doi.org/10.1109/TCST.2013.2271902.

[31] R. Horalek, J. Hlava, Multiple model predictive control of grid connected solid oxide fuel cell for extending cell life time, in: 2015 23rd Mediterranean Conference on Control and Automation, MED, 2015, pp. 310–315, http://dx.doi.org/10.1109/MED.2015.7158768.

[32] B. Zhang, F. Lin, C. Zhang, R. Liao, Y.-X. Wang, Design and implementation of model predictive control for an open-cathode fuel cell thermal management system, Renew. Energy 154 (2020) 1014–1024, http://dx.doi.org/10.1016/j.renene.2020.03.073, URL https://www.sciencedirect.com/science/article/pii/S0960148120303980.

[33] Z. Sun, Z. Chen, Y. Wang, H. Yuan, PEM fuel cell thermal management strategy based on multi-model predictive control, in: 2022 IEEE/IAS Industrial and Commercial Power System Asia (I&CPS Asia), 2022, pp. 625–630, http://dx.doi.org/10.1109/ICPSAsia55496.2022.9949807.

[34] Z. Liu, G. Chang, H. Yuan, W. Tang, J. Xie, X. Wei, H. Dai, Adaptive look-ahead model predictive control strategy of vehicular PEMFC thermal management, Energy 285 (2023) 129176, http://dx.doi.org/10.1016/j.energy.2023.129176, URL https://www.sciencedirect.com/science/article/pii/S0360544223025707.

[35] D. Hu, Y. Wang, J. Li, Q. Yang, J. Wang, Investigation of optimal operating temperature for the PEMFC and its tracking control for energy saving in vehicle applications, Energy Convers. Manage. 249 (2021) 114842, http://dx.doi.org/10.1016/j.enconman.2021.114842, URL https://www.sciencedirect.com/science/article/pii/S0196890421010189.

[36] X. Tang, Y. Zhang, S. Xu, Temperature sensitivity characteristics of PEM fuel cell and output performance improvement based on optimal active temperature control, Int. J. Heat Mass Transfer 206 (2023) 123966, http://dx.doi.org/10.1016/j.ijheatmasstransfer.2023.123966, URL https://www.sciencedirect.com/science/article/pii/S0017931023001217.

[37] Y. Qi, X. Li, S. Li, T. Li, M. Espinoza-Andaluz, P. Tunestål, M. Andersson, Temperature control strategy for polymer electrolyte fuel cells, Int. J. Energy Res. 44 (6) (2020) 4352–4365, http://dx.doi.org/10.1002/er.5209, arXiv:https://onlinelibrary.wiley.com/doi/pdf/10.1002/er.5209. URL https://onlinelibrary.wiley.com/doi/abs/10.1002/er.5209.

[38] Y. Cho, G. Hwang, D.Q. Gbadago, S. Hwang, Artificial neural network-based model predictive control for optimal operating conditions in proton exchange membrane fuel cells, J. Clean. Prod. 380 (2022) 135049, http://dx.doi.org/10.1016/j.jclepro.2022.135049, URL https://www.sciencedirect.com/science/article/pii/S0959652622046224.

[39] X.-H. Yuan, G. Wu, J.-G. Zhou, X. Xiong, Y.-P. Wang, MPC-based thermal management for water-cooled proton exchange membrane fuel cells, Energy Rep. 8 (2022) 338–348, http://dx.doi.org/10.1016/j.egyr.2022.10.236, URL https://www.sciencedirect.com/science/article/pii/S2352484722021734, Selected papers from 2022 7th International Conference on Advances on Clean Energy Research.

[40] J. Cao, C. Yin, R. Wang, R. Li, R. Liu, H. Tang, Dynamic thermal management of proton exchange membrane fuel cell vehicle system using the tube-based model predictive control, Int. J. Hydrog. Energy 70 (2024) 493–509, http://dx.doi.org/10.1016/j.ijhydene.2024.05.157, URL https://www.sciencedirect.com/science/article/pii/S0360319924018445.

[41] P.G. Anselma, S. Luciani, A. Tonoli, Predictive control framework for thermal management of automotive fuel cell systems at high ambient temperatures, IFAC- Pap. 55 (24) (2022) 298–303, http://dx.doi.org/10.1016/j.ifacol.2022.10.300, URL https://www.sciencedirect.com/science/article/pii/S2405896322023321, 10th IFAC Symposium on Advances in Automotive Control AAC 2022.

[42] C. Mayer, T. Eberhart, K. Huber, J. Karner, Fuel cell electric tractor powered with biogenic hydrogen - vehicle design and architecture, in: LAND. TECHNIK AgEng 2023, Vol. 2427, VDI Verlag, 2023, pp. 57–62.

[43] J. Konrad, C. Varlese, R. Krizan, C. Junger, P. Hofmann, Fuel cell electric powertrain for the agricultural tractor–FCTRAC: development, performance, and benchmarking, in: LAND. TECHNIK AgEng 2023, Vol. 2427, VDI Verlag, 2023, pp. 49–56.

[44] C. Varlese, A. Ferrara, C. Hametner, P. Hofmann, Experimental validation of a predictive energy management strategy for agricultural fuel cell electric tractors, Int. J. Hydrog. Energy 77 (2024) 1–14, http://dx.doi.org/10.1016/j.ijhydene.2024.06.097, URL https://www.sciencedirect.com/science/article/pii/S036031992402295X.

[45] C. Wang, M. Nehrir, S. Shaw, Dynamic models and model validation for PEM fuel cells using electrical circuits, IEEE Trans. Energy Convers. 20 (2) (2005) 442–451, http://dx.doi.org/10.1109/TEC.2004.842357.

[46] A. Goshtasbi, B.L. Pence, T. Ersala, Computationally efficient pseudo-2D non-isothermal modeling of polymer electrolyte membrane fuel cells with two-phase phenomena, J. Electrochem. Soc. 163 (13) (2016) F1412, http://dx.doi.org/10.1149/2.0871613jes.

[47] R. Vetter, J.O. Schumacher, Free open reference implementation of a two-phase PEM fuel cell model, Comput. Phys. Comm. 234 (2019) 223–234, http://dx.doi.org/10.1016/j.cpc.2018.07.023, URL https://www.sciencedirect.com/science/article/pii/S0010465518302807.

[48] J.C. Amphlett, R.M. Baumert, R.F. Mann, B.A. Peppley, P.R. Roberge, T.J. Harris, Performance modeling of the Ballard mark IV solid polymer electrolyte fuel cell: I . Mechanistic model development, J. Electrochem. Soc. 142 (1) (1995) 1, http://dx.doi.org/10.1149/1.2043866.

[49] T.M. Inc., 9.14.0.2206163 (r2023a), 2023, URL https://www.mathworks.com.

[50] A. De las Heras, F. Vivas, F. Segura, J. Andújar, From the cell to the stack. a chronological walk through the techniques to manufacture the PEFCs core, Renew. Sustain. Energy Rev. 96 (2018) 29–45, http://dx.doi.org/10.1016/j.rser.2018.07.036, URL https://www.sciencedirect.com/science/article/pii/S1364032118305446.

[51] Y. Wang, D.F. Ruiz Diaz, K.S. Chen, Z. Wang, X.C. Adroher, Materials, technological status, and fundamentals of PEM fuel cells – a review, Mater. Today 32 (2020) 178–203, http://dx.doi.org/10.1016/j.mattod.2019.06.005, URL https://www.sciencedirect.com/science/article/pii/S1369702119304948.

[52] O. Degrell, T. Feuerstein, DLG-Powermix - A practical tractor test, DLG test centre for agricultural machinery, Groß-Umstadt, Germany, 2003.

[53] P. Back, B. Hodel, P. Pirro, W. Stark, Replication of the DLG PowerMix Tractor Fuel Consumption Test in a Laboratory Environment, AgEng-Landtechnik 2011, Hannover, Germany, 2011.

[54] F. Borrelli, A. Bemporad, M. Morari, Predictive Control for Linear and Hybrid Systems, Cambridge University Press, 2017.

[55] L. Wang, Model Predictive Control System Design and Implementation Using MATLAB, Springer Verlag, 2009.

[56] J.B. Rawlings, D.Q. Mayne, Model Predictive Control: Theory and Design, 5th Edition, Wis. Nob Hill, 2015.

[57] J.A.E. Andersson, J. Gillis, G. Horn, J.B. Rawlings, M. Diehl, CasADi – a software framework for nonlinear optimization and optimal control, Math. Program. Comput. 11 (1) (2019) 1–36, http://dx.doi.org/10.1007/s12532-018-0139-4.

[58] A. Wächter, L.T. Biegler, On the implementation of an interior-point filter line-search algorithm for large-scale nonlinear programming, Math. Program. 106 (2006) 25–57, URL https://api.semanticscholar.org/CorpusID:14183894.